Oxygen Vacancy Formation on α-MoO_3 Slabs and Ribbons

Vishal Agarwal[†] and Horia Metiu[†*]

[†]Department of Chemistry & Biochemistry, University of California, Santa Barbara, California 93106-9510 USA

* Corresponding author; Phone:+1-805-893-2256; Fax: +1-805-893-4120; email: metiu@chem.ucsb.edu

citation of published version:

J. Phys. Chem. C 120 (25), 19252-19264 (August 17, 2016) DOI: 10.1021/acs.jpcc.6b06589

Abstract

MoO_3 is a versatile catalyst for oxidation reactions that consists of bilayers connected by van der Waals interaction. In principle a MoO_3 nanocrystal can be exfoliated to create two-dimensional ribbons. For this article, we study the difference between the chemistry of slabs having a variety of crystal faces and that of the edges of ribbons cut from a two-dimensional bilayer. As a descriptor of chemical reactivity we use the energy of oxygen-vacancy formation: the easier it is to form an oxygen vacancy, the better oxidant the face of a slab or the edge of a two-dimensional ribbon is. We find that the properties of ribbon edges are different from those of the corresponding slab surfaces. The surface energies of slabs are in the order $(010)_s < (100)_s < (101)_s < (001)_s$, whereas the edge energies of ribbons are in the order $<100>_r \sim <101>_r < <001>_r$ (the subscript s indicates a slab and r, a ribbon). Among the surfaces studied, we have found that $(001)_s$ and $(101)_s$ faces have the lowest oxygen-vacancy formation energies, and $(010)_s$ has the highest. In contrast, among the edges studied, $<101>_r$ has the lowest vacancy formation energies. Our calculations suggest that no benefit is obtained by creating $<100>_r$ or $<001>_r$ ribbon edges. However, a significant decrease of oxygen-vacancy formation energies is observed on formation of $<101>_r$ edge by exfoliating $(101)_s$ slabs. Also, among the structures studied, we found $<101>_r$ edges to be the most reactive and $(010)_s$ surfaces to be the least reactive.

1. Introduction

Recent experiments[1-5] have shown that layered compounds can be exfoliated (delaminated) to make two-dimensional materials. In particular, the exfoliation of α-MoO_3 has been achieved[4, 6-11] by a variety of methods. In this article we use density functional theory (DFT) to explore whether the catalytic properties of the two-dimensional MoO_3 produced by exfoliation are different from those of MoO_3 slabs. While we focus here on molybdenum oxide, the question of whether exfoliation produces new (hopefully better) catalysts is of more general interest because other oxides used in catalysis, such as V_2O_5, RuO_2, TiO_2, NiO, and CoO, can also be exfoliated.

There are several reasons for expecting that two-dimensional oxides will have different catalytic properties than the bulk materials. Corma[12-15] and Katz[16] have shown that the catalytic performance of delaminated zeolites is different from that of the same zeolite prior to delamination. Doped MoS_2, which is used as a catalyst in the oil industry, also seems to be a two-dimensional system whose activity is mainly at the border of the platelets.[17-19] It has been shown that *submonolayers* of molybdenum oxide supported on another oxide are better catalysts for methanol oxidation[20-30] or oxidative dehydrogenation of propane[23, 31-35] than MoO_3 powder. The catalytic activity deteriorates when more than a monolayer of molybdenum oxide is added to the support. These systems seem to indicate that two-dimensionality leads to different catalytic activity. Finally, it is the experience of much of chemistry that changes in morphology lead to changes in function, which is another reason for examining two-dimensional MoO_3.

Several ^{18}O isotope labelling studies have shown that the lattice oxygen is involved in oxidation reactions catalyzed by metal oxides,[36-39] as assumed in the Mars-van Krevelen mechanism.[40-42] The energy of oxygen-vacancy formation has been used as a predictor of the ability of surface oxygen to engage in chemical reactions with reductants.[43-45] It is for this reason that we compare here the energy of oxygen-vacancy formation on the surface of MoO_3 slabs, on a two-dimensional sheet that extends to infinity in both direction, and on two-dimensional ribbons that are bilayers that extend to infinity in one direction and are finite in the other. The delamination of α-MoO_3 is possible because the bulk is a layered compound consisting of two atomic layers (which we call a bilayer) which are held together by chemical bonds. The MoO_3 crystal consists of bilayers held together by van der Waals forces. Therefore, we expect that exfoliation will generate bilayers and this is why we study bilayers rather than monolayers.

α-MoO_3 has found applications in electronic devices,[46-47] battery electrodes,[48-50] optical devices,[51-52] and gas sensors.[7, 53-55] The presence of oxygen vacancies will affect the performance in these applications.

Previous computational work[56-73] on MoO_3 was performed for the (010) surface. This is the cleavage plane and therefore is expected to have the lowest surface energy and be predominantly present in MoO_3 crystallites. However, having lowest surface energy also suggests that this face might be the least reactive. Other faces, which have higher surface

energy, hence a lower area in the crystallite, might be more active and might dominate catalytic activity. For this reason we study oxygen-vacancy formation energies on (010), (100), (001), and (101) faces. More importantly, we address in this work how reactivity changes when these surfaces become edges in a two-dimensional ribbon of MoO_3 bilayers prepared by exfoliation.

The remainder of this article is organized as follow. In Section 2 we briefly describe the models of slabs and ribbons of α-MoO_3 along with computational details. In Section 3, we discuss results of oxygen-vacancy formation on various surfaces and edges. Section 4 is a summary of the results.

2. Methodology

2.1. Models

Bulk α-MoO_3. α-MoO_3 is the most stable form of molybdenum trioxide. It has orthorhombic structure (space group *Pbnm*) and is composed of bilayers perpendicular to the [010] direction, interacting through van der Waal's forces.[74-75] Each bilayer consists of two layers of corner- and edge-sharing distorted [MoO_6] octahedrons as shown in Figure 1. (An interactive 3D model of MoO_3 is given in the Supporting Information, Figure S11.) In the [001] direction the octahedrons are connected by edges (two oxygens are shared) and in the [100] direction they are connected by corner oxygen atoms (one O atom is shared). The primitive unit cell (PUC) consists of *four* [MoO_3] units. For studying [101], [010], and [$\bar{1}$01] surfaces and edges, a transformation matrix was applied to PUC to change the basis vectors. The new unit cell ("UC1") consists of *eight* [MoO_3] units.

α-MoO_3 has three crystallographically distinct oxygen atoms (see Figure 1): a singly coordinated terminal oxygen (O_t) which makes a double bond with a Mo atom (this M=O group is sometimes called a molybdyl), a 2-fold coordinated asymmetric oxygen (O_a), and a 3-fold coordinated symmetric oxygen (O_s). O_a forms one long bond (2.18 Å) and one short bond (1.75 Å) with two Mo atoms in the same layer. O_s on the other hand forms two equal bonds (1.95 Å) to Mo atoms in the same layer and has a much longer bond with a Mo atom in another layer.

To determine the U-parameter for the DFT+U calculation, we calculate the energy of conversion of MoO_2 to MoO_3 (see below). MoO_2 has a distorted rutile structure with a monoclinic unit cell (space group *P2_1/c*).[76-77] The primitive unit cell of MoO_2 consists of *four* [MoO_2] units. Bonding in MoO_2 is complex and may be explained through a Goodenough

model.[78] In a nutshell, MoO_2 (d^2) shows both metallic conductivity (due to partial filling of the M-O π^* band) and metal-metal bonding (due to filling of the Mo-Mo σ band preferring the formation of metal-metal dimers, and hence the distorted rutile structure). We do not intend to study MoO_2 except for the fact that we need its energy for determining the value of U (see Section 2.2).

The models used for α-MoO_3 slabs are shown in Figure 2. Only the lowest energy surfaces are shown here. To determine the lowest energy structures we studied a larger number of systems, which are shown in the Supporting Information (Figures S1, S2, and S3). In what follows we use the subscript s for slab faces. For example, *slabs* exposing to vacuum the surface perpendicular to [010] direction are labeled $(010)_s$. Two possible ways to form a (100) surface are shown in Supporting Information (Figure S1). We find that cutting along a weaker (and hence longer) Mo-O_a bond produces surfaces (or edges) with lowest energy (see Supporting Information Figure S1).

For studying the (100), (010), and (001) surfaces, a supercell was obtained by repeating PUC four times in the [100] and [001] directions. For preparing (101) surfaces, UC1 was repeated three times in the [101] and $[\bar{1}01]$ directions. The $(\bar{1}01)$ surface is identical to the (101) surface and therefore we only studied (101). The slab thickness used in calculations was sufficient to converge surface energies (convergence data is not shown). We provide interactive 3D models of lowest energy slab in the Supporting Information (Figure S12).

α-MoO_3 Sheets and Ribbons. In what follows we use the word 'sheet' for a bilayer that extends to infinity in two directions. A ribbon is a bilayer that extends to infinity in one direction (Figure 3a shows a schematic representation of a ribbon). α-MoO_3 sheets are constructed by exfoliating α-MoO_3 slabs along [010] to a single bilayer and then re-optimizing. Since in the bulk MoO_3 the bilayers are connected by van der Waals interactions, we do not expect that the reactivity of a two-dimensional sheet is very different from that of a (010) slab containing more than one sheet. The models used for α-MoO_3 ribbons are shown in Figure 3. Only lowest energy edges are shown here. For all possible cuts to form edges, see Supporting Information (Figures S4, S5, and S6). Ribbons are labeled by angle brackets with a subscript 'r'. For example the ribbon having an edge along the [100] direction is denoted by $<100>_r$. For the

lowest energy ribbon, we also provide an interactive 3D model in the Supporting Information (Figure S13).

For slabs and ribbons, a vacuum of 14 Å is added along the cut and/or cleavage direction, to decouple the images from each other. For example, a vacuum of 14 Å is added along [010] and [100] directions for the $<100>_r$ ribbon.

2.2. Computational details

Spin-polarized density functional theory (DFT) calculations were performed with the Vienna *ab initio* program (VASP),[79-82] using the Perdew-Burke-Ernzerhof (PBE) functional[83] and the projector-augmented-wave (PAW) method.[84] The frozen-core approximation was used with a cutoff radius of 0.804 Å and 1.429 Å for O and Mo atoms, respectively. Six electrons ($[2s^2 2p^4]$) for O atom and twelve electrons ($[4p^6 5s^1 5d^5]$) for Mo atom were treated explicitly. The effect of the other electrons was included through the default PAW pseudo-potential.

Periodic boundary conditions were applied in all the directions.[85] Van der Waal forces were incorporated using the pair-additive Grimme D2 method.[86] The DFT+U method with Dudarev's approximation[87] was used to compensate for the self-interaction error in the PBE functional. We used a value of 2 eV for U_{eff} (where $U_{eff} = U - J$) for *d*-orbitals of Mo atom which we derived to fit the reduction energy of the oxide, the unit cell parameters, and the magnetic moments (see Section 2.3).

Full geometry relaxations were performed until the maximum force on each atom was less than 0.02 eV/Å. The iterations in the electronic energy calculation were stopped when the total energy change was less than 10^{-5} eV. The calculated cell parameters of α-MoO_3 and Mo-O bond lengths with $U_{eff} = 2$ eV are in good agreement with the experimental results (see Table 1 and Table 2). Volume optimization calculations were performed for the bulk structures using a plane-wave energy cutoff of 500 eV. The initial structures in optimization were that given by XRD. Thereafter, i.e. for ribbons and slabs, production runs were performed with a plane-wave energy cutoff of 400 eV with fixed simulation cell parameters obtained from volume relaxation at higher cutoff.

For benchmarking purposes we have also used the hybrid Heyd-Scuseria-Ernzerhof (HSE06) functional.[88-90] For the HSE06 functional, geometry optimizations were performed at fixed cell parameters obtained from experiments.

The k-point mesh was chosen to satisfy the relation k-point × simulation cell length > 25 Å, along each cell direction. For example, for a simulation cell of dimensions 30 Å × 15 Å × 15 Å, we used a k-point mesh of 1 × 2 × 2. The k-points chosen by this methodology lead to converged oxygen-vacancy energies. The energies of gas-phase H_2, O_2, and H_2O were computed using a cubic box of length 15 Å. We observed no change in energy on increasing the box length to 20 Å.

The Bader charge on each atom was calculated with an algorithm developed by Henkelman *et al*.[91] Surface energies were computed using the relation:

$$E_{\text{surf}} = \frac{1}{2A}\left[E_{\text{slab}}(n_s) - n_s E_{\text{bulk}}\right], \quad (1)$$

where E_{bulk} is the energy of the bulk α-MoO_3 per [MoO_3] unit, n_s is number of MoO_3 units in the α-MoO_3 slab, A is the surface area of the slab, and E_{slab} is the total energy of the α-MoO_3 slab. Edge energies of a ribbon were calculated using the relation:

$$E_{\text{edge}} = \frac{1}{2L}\left[E_{ribbon}(n_r) - n_r E_{sheet}\right], \quad (2)$$

where E_{sheet} is the energy of the (010) α-MoO_3 infinite two-dimensional sheet per unit of [MoO_3], n_r is number of [MoO_3] units in the α-MoO_3 ribbon, L is the length of the edge of the ribbon, and E_{ribbon} is the total energy of the ribbon. Using E_{sheet} as reference removes surface energy and gives only the energy attributed to the edge.

2.3. Estimation of U_{eff}

A wide variety of U_{eff} values falling in the range of 1-8.3 eV has been used in the literature.[57, 59-60, 92-96] The value of U_{eff} depends on the quantities being fitted since it is unlikely that one can find a value of U_{eff} that will give correct results for all measurable properties. Here we are interested in computing total energies and we chose[100,102] U_{eff} to fit the energy of the reaction $MoO_3 + H_2 \rightarrow MoO_2 + H_2O$. In addition, we required that U_{eff} should also give correct values for the cell parameters and the magnetic moment of MoO_2 calculated by HSE. We note here that the range of U_{eff} studied in this work does not affect the magnetic moment on Mo atom in MoO_3 crystal, however, have significant effect in MoO_2 crystal.

Figure 4 shows the change of the energy of the reaction $MoO_3 + H_2 \rightarrow MoO_2 + H_2O$ (denoted by "ΔE" in Figure 4a), of the lattice parameters a/γ (Figure 4b) and b/c (Figure 4c), and

of the magnetic moment as a function of U_{eff}. In these calculations U_{eff} was varied between 1 and 8 in increments of 1. Spin-polarized PBE with U_{eff} = 2 eV gives good fits to all four quantities. Figure 4d suggests that MoO_2 is anti-ferromagnetic, whereas experiments near room temperature suggest MoO_2 is Pauli-paramagnetic.[97-99] We are not aware of any study that has measured magnetic susceptibility of MoO_2 at 0 K, which is what our calculations give. MoO_2 may be antiferromagnetic at very low temperatures and Pauli-paramagnetic at high temperatures. Such behavior has been previously observed for NiS.[100]

3. Results and Discussion

3.1. Structures and energies of surfaces of slabs and of edges of ribbons

The $(010)_s$ face. The notation $(010)_s$ indicates the (010) face of a slab (the subscript s indicates that the structure is a slab and not a ribbon). As discussed before, α-MoO_3 consists of (010) bilayers interacting with van der Waals forces. Thus, creating a $(010)_s$ surface does not require breaking chemical bonds. We have studied one and two bilayers of α-MoO_3. As seen in Table 2, we find (as found previously[57]) negligible difference in the bond lengths and Bader charges between one bilayer, two bilayers, and bulk α-MoO_3. This is not surprising: bulk α-MoO_3 can be cleaved to expose this face.

The $(100)_s$ face and the $<100>_r$ edge. We use the symbols $(100)_s$ for the (100) face of a slab and $<100>_r$ for the edge of a ribbon that ended on the (100) face of the slab being laminated. The (100) face is obtained by cutting Mo-O_a bonds (the meaning of various subscripts for oxygen are explained in Figure 1). The structures of $(100)_s$ and $<100>_r$, after geometry optimization, are shown in Figure 2c and Figure 3b, respectively. The changes in the Mo-O bond lengths in [MoO_6] octahedra are shown in Figure 5. Cutting Mo-O_a bonds to create the (100) face or the $<100>_r$ ribbon exposes: (a) under-coordinated O_a in one sub-layer and (b) Mo in the other. Upon optimization, the under-coordinated oxygen forms a double bond with a Mo atom located in the same (010) plane (the Mo-O bond decreases from 1.75 Å to 1.68 Å). It is not surprising that previous studies have found an increase in intensity of Mo=O Raman peak (~ 990 cm^{-1}) on increase in surface area of (100) surface.[101] The exposed Mo center assumes a distorted square-pyramidal geometry and strengthens bonds with nearby oxygens (the most significant being decrease in Mo-O_s bond length from 2.41 Å to 2.17 Å along [010] sub-layers). We find

negligible difference in bond lengths between the $(100)_s$ surface and $<100>_r$ edge as shown in Figure 5.

The $(001)_s$ face and the $<001>_r$. $(001)_s$ and $<001>_r$ are created by cutting Mo-O_s bonds (for oxygen labeling see Figure 1). The structures of $(001)_s$ and $<001>_r$, after geometry optimization, are shown in Figure 2e and Figure 3d, respectively. We compare changes in the Mo-O bond lengths in [MoO_6] octahedra in Figure 6. Cutting of Mo-O_s bond exposes: (a) under-coordinated O_s on one [010] sub-layer and (b) Mo on the other. Upon optimization the under-coordinated oxygen strengthens its interaction with exposed Mo on the other (010) sublayer (resulting in a decrease in Mo-O_s bond from 2.41 Å to ~ 1.9 Å). The exposed Mo atom assumes a distorted square-pyramidal geometry. The atoms on the $<001>_r$ edge have room to relax in the [010] direction. As a result, the Mo-O_s on the octahedral molybdenum center on the edge has a longer bond length (~ 3.79 Å), compared to that on $(001)_s$ surface (~ 3.11 Å). Apart from that, we find negligible difference in bond lengths between the $(001)_s$ surface and the $<001>_r$ edge (see Figure 6).

The $(101)_s$ face and the $<101>_r$ edge. The creation of the $(101)_s$ face or of the $<101>_r$ ribbon requires cutting Mo-O_s and Mo-O_t bonds (for the definition of the subscripts on oxygen see Figure 1), as shown in Figure 7. This exposes: under-coordinated O_s and O_a on one (010) sub-layer and Mo on the other. Upon optimization, each under-coordinated O_a atom forms a double bond with a Mo atom located in the same (010) plane (indicated by decrease in Mo-O bond from 1.75 Å to 1.69 Å); and O_s strengthens its interaction with exposed Mo on the other (010) sublayer (indicated by decrease in Mo-O_s bond from 2.41 Å to ~1.84 Å). Because of more conformational freedom in [010] direction, we find a longer bond length of Mo-O_s on the $<101>_r$ edge (~ 3.52 Å) as compared to that on $(101)_s$ surface (~ 3.09 Å). Apart from that, we find negligible difference in bond lengths between relaxed $(101)_s$ surface and $<101>_r$ edge as shown in Figure 7.

Surface and edge energies. α-MoO_3 crystals grown under low pressures by vapor condensation are thin flat bars, with $(010)_s$ as the flat face and elongated along the [001] direction.[102] Indeed, as shown in Figure 2, we find that $(010)_s$ surface has the lowest surface energy, followed by

$(100)_s$. Note that we compute surface energies in vacuum under the assumption that the surface does not have oxygen vacancies, or steps, or adsorbates (e.g. hydroxyls). None of these assumptions is valid for crystals grown in the laboratory. Because of this, one should not expect that the equilibrium shape produced by Wulff's construction—based on the calculated surface energies—will match the shapes obtained in experiments. However, it happens that in this particular case our computational results produce qualitatively similar picture of the crystal structure as obtained from the experiments.

The edge energies are 0.218 eV/Å for $<100>_r$, 0.278 eV/Å for $<001>_r$, and 0.218 eV/Å for $<101>_r$. Interestingly, the edge energy of $<101>_r$ is nearly equal to that of $<100>_r$, while this equality does not take place for (101) and (100) faces. This is because exfoliated $<101>_r$ has more room to relax in the [010] direction as compared to $(101)_s$.

3.2. Oxygen Vacancy Formation

We report oxygen-vacancy formation energies (ΔE_o) with respect to formation of half a O_2 molecule, i.e., $\Delta E_0 = E_{vac} + ½\, E_{O2} - E_{st}$. Here E_{vac} is the energy of a surface (or edge) with one oxygen vacancy per supercell, E_{O2} is the energy of the gas phase O_2 molecule, and E_{st} is the energy of the same supercell with no vacancy (the subscript st stands for stoichiometric). Because the binding energy of O_2 calculated by PBE is erroneous, we put little emphasis on the absolute magnitude of vacancy formation energies but assume that the relative values are meaningful because the difference between energy of formation of two different oxygen vacancies (i.e. O is removed from two different locations) does not depend on the energy of the gaseous oxygen.

When an oxygen atom is removed from an oxide, to form an oxygen vacancy, two "unpaired electrons" are left behind in the reduced oxide. Previous calculations for TiO_2[103-104] and CeO_2[105-106] have shown that these two unpaired electrons will be localized on two cations reducing them: the formation of one vacancy produces two Ti^{3+} or two Ce^{3+}. In the case of MoO_3 the situation is more complicated because: (1) the two electrons left behind could both go on one Mo ion creating an ion with formal charge 4+; or the two electrons can go on two different Mo ions creating two ions with formal charge 5+; or they can be delocalized over a group of ions; and (2) the location of the reduced ions with respect to the oxygen-vacancy site and with respect to each other also needs to be studied since these locations did affect the energy of oxygen-

vacancy formation on TiO_2[103-104] or CeO_2. We have not explored the dependence of the oxygen-vacancy formation on the location of the reduced ions because this would require an extremely large number of calculations (for example, in the case of TiO_2, Chrétien and Metiu[104] examined 80 different possibilities).

In the present study we proceeded as follows. When a bridging oxygen is removed we initialized the magnetic moments on the two Mo atoms that were bridged by the lost oxygen to be equal to +1 μ_B. This means that prior to optimization the two Mo atoms that lost the oxygen atom bridging them are in a 5+ formal state. After that we allow the ions and the electrons to evolve so that a minimum in the total energy is reached. If the magnetic moment on the two Mo atoms is still 1 μ_B we conclude that the unpaired electrons are localized on the two Mo atoms making them Mo^{5+}. Alternatively, when the oxygen from the molybdenyl is removed we set the initial magnetic moment on the Mo atom that lost the oxygen to 2 μ_B and proceed with the optimization. The final location of unpaired electrons is interpreted using combination of HOMOs and Bader charges (as discussed below). We find below unpaired electrons localized either on single Mo atom (giving Mo^{4+}) or on two Mo atoms (giving 2 Mo^{5+}) or on several Mo atoms in which case we say that they are delocalized (this does not mean that they form a band, because they do not). Experimentally, several XPS studies[55, 107-110] concluded that both Mo^{4+} and Mo^{5+} are present in the reduced α-MoO_3 and there are EPR studies[55, 108, 111] claiming that Mo^{5+} is also present.

3.2.1. (010) α-MoO_3 Sheets and Slabs

The oxygen-vacancy formation energies on all the systems studied here are given in Table 3. For the $(010)_s$ face, we find that O_a is easiest to remove, followed by O_t; there is no difference in vacancy formation energies in 1-bilayer and 2-bilayers. Previous calculations, which did not use DFT+U, found that the energy to remove O_t is very close to the energy to remove O_a.[56, 58, 112] Calculations using DFT+U (U_{eff} = 6.3 eV), found that O_t is easier to remove.[57, 60] However, the experiments reported by Smith and Ozkan[101, 113] suggest that O_a is easier to remove, which is in qualitative agreement with the present calculations.

The density of states (DOS) of stoichiometric (010) bilayers and the bilayer with an oxygen vacancy are shown in Figure 8. Figure 8b shows the density of states when either an O_a or an O_t is removed. They are shown together because when we remove O_t (which is a molybdenyl

oxygen) a neighboring bridging oxygen O_a moves to replace the atom that was removed (thus recreating the molybdenyl). As a result the vacancy created by O_t is the same as the one formed when we remove O_a. The removal of O_t causes the formation of two degenerate orbitals with opposite spins and with the energy in the band gap. The equal density surface for the two orbitals is shown at the right-hand side of the Figure 8b. The location of the oxygen vacancy is shown in yellow. The two orbitals have the same energy and identical shape and differ only through the spin of the electron. They spread over several Mo atoms (green) and are mainly a combination of Mo *d*-orbitals. The delocalization of these electrons is also reflected by the change of the Bader charge on these Mo atoms (from 2.69 to 2.5-2.55). It is interesting to note that the distribution of the unpaired electrons is along the [100] direction: in our previous work we showed that is causes an anisotropy in the surface which will cause a preference for a certain distribution of vacancies on the surface.[73]

Figure 8c shows the density of states after the removal of O_s. The removal causes the formation of two degenerate orbitals whose energy is in the band-gap. A plot of these orbitals (which differ only through the spin of the electron) is shown at the right-hand side of the panel. The unpaired electrons are now localized on the two Mo atoms that were bridged by the removed oxygen atom. We interpret this to mean that two Mo^{6+} were converted to Mo^{5+}. This formal charge assignment is also supported by a decrease in the Bader charge. The bottom panel shows the density of states for a state of higher energy obtained by removing an O_t and starting the calculation with 2 μ_B on the Mo atom that lost oxygen. In this case the formation of the vacancy creates two non-degenerate states in the gap both with spin up. Essentially the difference between the vacancy formed in the (b) panel and the one formed in the (d) panel is that one is a "singlet" state and the other is a "triplet". The energy of forming the triplet vacancy is higher than that for forming the singlet. The pictures of these two orbitals show that the unpaired electrons are essentially located on the Mo atom that lost oxygen. We interpret this to mean that the molybdenum atom that lost the molybdenyl has a formal charge of 4+. This assignment is supported by the fact that the Bader charge on this molybdenum atom is 2.15, which is very close to the charge of 2.12 of the Mo atom in a MoO_2 crystal.

3.2.2. α-MoO_3 Slabs and Ribbons

Here, we compare oxygen-vacancy formation energies (ΔE_o) on the surface of a slab and the corresponding edge of the ribbon. We provide the lowest vacancy formation energies in Table 3. The complete list of oxygen-vacancy formation energies is given in Supporting Information (Table S1). On surface of the slab we only studied vacancy formation by removing those oxygen sites which had lowest ΔE_o on the corresponding edge of the ribbon. For example, we only studied removal of O(2) from $(100)_s$ surface because removal of O(2) has the lowest energy on the $<100>_r$ edge. (A subscript 'r' denotes ribbon and subscript 's' denotes slab.) Also, we note that oxygens are labelled as O(1) , O(2), … , O(n) which are shown in Figures 2 and 3.

The $(100)_s$ face and the $<100>_r$ edge. We studied removal of *five* different types of oxygen on the $<100>_r$ edge labelled in Figure 3b. Among these five oxygens on the $<100>_r$ edge, we find O(1) or O(2) are the easiest to remove. The energies of oxygen removal are given in Table 3 (see Table S1 in Supporting Information for complete list of energies of oxygen removal). We also provide density of states and partial charge density plots after oxygen removal in Figure S8. We note here that removing O(1) and O(2) leads to the same final geometry (magenta in Figure 3b), and hence the same vacancy formation energies. The final geometry after optimization of $<100>_r$ with O(2) vacancy is shown in Figure 9. We show removed oxygen with yellow sphere. On removal of O(2), we find that the molybdenum —which lost its oxygen atom— strengthens its bond with neighboring O_a (indicated by decrease in bond length from 2.17 Å to 1.74 Å). The removal of O(2) leaves behind two electrons. The two electrons localize on the next nearest and the next-next nearest neighbors along [100] direction. This can be seen from the HOMOs in Figure 9a). In this case, the formation of the vacancy creates two degenerate states which are located in the band gap (see density of states plots in Figure S8 in the Supporting Information). To confirm the state of Mo atoms, we performed Bader charge analysis and found a decrease in Bader charge on these Mo atoms from 2.6 to 2.4. We interpret these results to mean that the two Mo atoms which were formally 6+ have converted to 5+.

For the surface **$(100)_s$** , O(2) can be found in two different environments (labelled as O(2) and O'(2) in Figure 2c). ΔE_o for vacancy of both these oxygens are within PBE error (0.07 eV) and therefore we were not able to decide which is easier to remove (see Table 3). We now compare ΔE_o for O(2) vacancy on the $(100)_s$ slab to that on the $<100>_r$ edge. We find that the difference is ~ 0.05 eV. Within the error of PBE, the two energies are equal and hence removal

of O(2) on $(100)_s$ and $<100>_r$ will yield the same effect. This is not surprising given that we found negligible differences in the bond lengths between the $(001)_s$ surface and the $<001>_r$ edge (see Figure 5 and Section 3.1).

The $(001)_s$ face and the $<001>_r$ edge. Out of the *five* different types of oxygen studied (see Figure 3d for labelling) on $<001>_r$ edge, we find that O(2) or O(5) (shown in magenta in Figure 3d) are easiest to remove. The energy to remove these oxygens is the same because they gave the same final geometry. The energy to remove O(1) or O(3) is nearly 0.2 eV higher than that of O(2) or O(5) (again they both yielded the same final geometry on optimization), which is within PBE error. Therefore, we were not able to decide which of them is easiest to remove. Hence we studied removal of both O(3) and O(3) on the surface of $(001)_s$.

In Table 3, we compare vacancy formation energies on O(3) and O(5) on the edge of $<001>_r$ to that on the surface of $(001)_s$. The complete list of oxygen-vacancy formation energies are provided in Supporting Information in Table S1. The results show that it requires ~ 0.7 eV less energy to remove an O(3) from the $(001)_s$ surface than from the $<001>_r$ edge. Therefore, we predict that $(001)_s$ surface will be more active than $<001>_r$ edge. As shown in Figure 6 and discussed in Section 3.1, there are significant structural differences between $<001>_r$ edge and $(001)_s$ surface and therefore, this observation is not surprising.

The final geometries, after the optimization of the $<001>_r$ ribbon with O(3) vacancy and of the $(001)_s$ slab with O(3) vacancy are shown in Figures 10a and 10b, respectively. The removal of O(3) causes a complex reconstruction on both the edge of the ribbon and on the surface of the slab. The molybdenyls on the $<100>_r$ edge have more freedom to relax in the [010] direction as compared to those on the $(001)_s$ face. Thus, oxygen-vacant $<100>_r$ ribbon and $(001)_s$ slab show considerable differences in relaxed structures as shown in Figure 10. The differences in the initial and final geometries results in vastly different oxygen-vacancy formation energies.

Next we investigated the location of excess electrons after removal of oxygen. Again, we use combination of partial charge densities of the states in the band gap and Bader charges to interpret the location of excess of electrons. Interestingly, we find that excess electrons in case of the oxygen-vacant $<100>_r$ are delocalized on several Mo atoms (see Figure S9 in the Supporting Information), whereas removal of oxygen on $(001)_s$ face produces two Mo^{5+} atoms. The molybdenum atoms having excess electrons on $(001)_s$ face are numbered in Figure 10b).

The $(101)_s$ face and the $<101>_r$ edge. We studied removal of *four* different oxygens on the edge of $<101>_r$ labelled in Figure 3d. On a $<101>_r$ ribbon, we find O(3) is easiest to remove (see Table S1 in Supporting Information). We find that removal of O(3) oxygen from the surface of $(101)_s$ requires ~0.8 eV more energy (see Table 3). Again, this observation is not surprising given that there are significant differences in the initial structure of $(101)_s$ surface and $<101>_r$ edge (see Figure 7 and Section 3.1). This result indicates that it would be beneficial to exfoliate MoO_3 if a more active Mars-van Krevelen catalyst is desired. Also, we find that among all the surfaces (or edges) considered $(101)_s$ surface (or $<101>_r$ edge) contain the most reactive oxygen (see Table S1 for complete list of oxygen vacancies studied in this work).

The final geometries after removal of O(3) are shown in Figure 11. We also provide final geometries after removal of O(1) and O(2) in Supporting Information Figure S10. On both $(101)_s$ surface and $<101>_r$ edge, the removal of these oxygen atoms causes a complex reconstruction that is not limited to small, local relaxations of atomic positions as shown in Figure 11. Again, we mention that it is the vastly different initial and final geometries that result in significantly different oxygen-vacancy formation energies. Upon investigating excess electron localization (using partial density plots of states in the band gap and Bader charges), we find that, for both the reduced $<101>_r$ and the reduced $(101)_s$, the electrons left behind after the removal of the oxygen atoms are delocalized over several Mo atoms.

4. Conclusions

For this article, we investigated differences in structures and oxygen-vacancy formation energies of various α-MoO_3 surfaces of slabs and on the edges of ribbons. We performed DFT+U calculations with $U_{eff} = 2$ eV for Mo atom. This value of U_{eff} was obtained by fitting the reduction energy of MoO_3 with H_2, the lattice parameters of MoO_2, and the HSE magnetic moment of Mo atoms in a unit cell of MoO_2.

We find negligible structural differences in bond lengths on $(100)_s$ slabs compared to that on $<100>_r$ ribbon obtained after exfoliation. However, there are significant differences in bond lengths for $(001)_s$ and $(101)_s$ slabs compared to those on ribbons.

The surface energies of slabs are in the order $(010)_s < (100)_s < (101)_s < (001)_s$, whereas the edge energies of ribbons are in the order $<100>_r \sim <101>_r < <001>_r$.

O_a (asymmetric bridging oxygen) or O_t (terminal molybdenyl) are easiest to remove on a stoichiometric $(010)_s$ surface. Among the different surfaces studied, we find that $(001)_s$ and $(101)_s$ faces have the lowest oxygen-vacancy formation energies and $(010)_s$ has the highest. Among the edges studied, we find that $<101>_r$ has the lowest vacancy formation energies. This is not surprising given that several experimental studies have previously reported catalytic anisotropy of α-MoO_3.[101, 114-118]

We find that no benefit is obtained by creating <100> and <001> edges. However, a significant decrease of oxygen-vacancy formation energies is observed on formation of $<101>_r$ edge by exfoliating $(101)_s$ slabs. Among all the structures studied in this work, we find $<101>_r$ has the lowest oxygen-vacancy formation energies, and therefore we predict $<101>_r$ edges to have the highest reactivity for Mars-van Krevelen type reactions.

All in all we suggest if one desires to make a MoO_3 ribbon that is a milder oxidant, one should minimize the length of the $<101>_r$ edges. Alternatively, when a strong oxidant is desired formation of $<101>_r$ edges should be maximized.

Supporting Information. Surface and edge preparation; complete list of oxygen vacancy formation energies; side views of O(1), O(2) and O(3) vacancy on $<101>_r$; edge and top views of O(1), O(2) and O(3) vacancy on $(101)_s$ slab; density of states plots for vacancies on $<100>_r$, $<001>_r$, and $<101>_r$ edges; and interactive 3D models of MoO_3 bulk, MoO_3 slabs and MoO_3 ribbons. This material is available free of charge via Internet at http://pubs.acs.org.

Acknowledgments. We thank Dr. Henrik Kristoffersen for stimulating discussions and Dr. Gregory Mills for codes on unit cell transformation. We acknowledge support from the Center for Scientific Computing at the California NanoSystems Institute and the UCSB Materials Research Laboratory (an NSF MRSEC, DMR-1121053) funded in part by NSF CNS-0960316 and Hewlett-Packard, and from the Department of Energy, Office of Science, Office of Basic Energy Sciences DE-FG03-89ER14048.

References

(1) Nicolosi, V.; Chhowalla, M.; Kanatzidis, M. G.; Strano, M. S.; Coleman, J. N. Liquid Exfoliation of Layered Materials. *Science* **2013,** *340*, 1226419-1226419.

(2) Xiao, H.; Chaoliang, T.; Zongyou, Y.; Hua, Z. 25th Aniversary Article: Hybrid Nanostructures Based on Two-Dimensional Nanomaterials. *Adv. Mater.* **2014,** *26*, 2185-2204.

(3) Young, R. J. Two-Dimensional Nanocrystals: Structure, Properties and Applications. *Arabian J. Sci. Eng.* **2013,** *38*, 1289-1304.

(4) Smith, R. J.; King, P. J.; Lotya, M.; Wirtz, C.; Khan, U.; De, S.; O'Neill, A.; Duesberg, G. S.; Grunlan, J. C.; Moriarty, G., et al. Large-Scale Exfoliation of Inorganic Layered Compounds in Aqueous Surfactant Solutions. *Adv. Mater.* **2011,** *23*, 3944-3948.

(5) Ma, R.; Sasaki, T. Nanosheets of Oxides and Hydroxides: Ultimate 2d Charge-Bearing Functional Crystallites. *Adv. Mater.* **2010,** *22*, 5082-5104.

(6) Li, F. Y.; Chen, Z. F. Tuning Electronic and Magnetic Properties of MoO_3 Sheets by Cutting, Hydrogenation, and External Strain: A Computational Investigation. *Nanoscale* **2013,** *5*, 5321-5333.

(7) Alsaif, M. M. Y. A.; Balendhran, S.; Field, M. R.; Latham, K.; Wlodarski, W.; Ou, J. Z.; Kalantar-zadeh, K. Two Dimensional α-MoO_3 Nanoflakes Obtained Using Solvent-Assisted Grinding and Sonication Method: Application for H_2 Gas Sensing. *Sensors and Actuators B* **2014,** *192*, 196-204.

(8) Kumar, V.; Sumboja, A.; Wang, J.; Bhavanasi, V.; Nguyen, V. C.; Lee, P. S. Topotactic Phase Transformation of Hexagonal MoO_3 to Layered MoO_3 -II and Its Two-Dimensional (2d) Nanosheets. *Chem. Mater.* **2014,** *26*, 5533-5539.

(9) Murugan, a. V.; Viswanath, A. K.; Gopinath, C. S.; Vijayamohanan, K. Highly Efficient Organic-Inorganic Poly(3,4-Ethylenedioxythiophene)-Molybdenum Trioxide Nanocomposite Electrodes for Electrochemical Supercapacitor. *J. Appl. Phys.* **2006,** *100*, 074319.

(10) Tagaya, H.; Ara, K.; Kadokawa, J.-i.; Karasu, M.; Chiba, K. Intercalation of Organic Compounds in the Layered Host Lattice MoO_3. *J. Mater. Chem.* **1994,** *4*, 551.

(11) Hanlon, D.; Backes, C.; Higgins, T. M.; Hughes, M.; O'Neill, A.; King, P.; McEvoy, N.; Duesberg, G. S.; Mendoza Sanchez, B.; Pettersson, H., et al. Production of Molybdenum Trioxide Nanosheets by Liquid Exfoliation and Their Application in High-Performance Supercapacitors. *Chem. Mater.* **2014,** *26*, 1751-1763.

(12) Corma, A.; Fornes, V.; Pergher, S. B.; Maesen, T. L. M.; Buglass, J. G. Delaminated Zeolite Precursors as Selective Acidic Catalysts. *Nature* **1998,** *396*, 353-356.

(13) Corma, A.; Fornés, V.; Martínez-Triguero, J.; Pergher, S. B. Delaminated Zeolites: Combining the Benefits of Zeolites and Mesoporous Materials for Catalytic Uses. *J. Catal.* **1999,** *186*, 57-63.

(14) Corma, A.; Diaz, U.; Domine, M. E.; Fornés, V. New Aluminosilicate and Titanosilicate Delaminated Materials Active for Acid Catalysis, and Oxidation Reactions Using H_2O_2. *J. Am. Chem. Soc.* **2000,** *122*, 2804-2809.

(15) Corma, A.; Fornés, V.; Guil, J. M.; Pergher, S.; Maesen, T. L. M.; Buglass, J. G. Preparation, Characterisation and Catalytic Activity of ITQ-2, a Delaminated Zeolite. *Microporous Mesoporous Mater.* **2000,** *38*, 301-309.

(16) Katz, M. B.; Graham, G. W.; Duan, Y. W.; Liu, H.; Adamo, C.; Schlom, D. G.; Pan, X. Q. Self-Regeneration of Pd-$LaFeO_3$ Catalysts: New Insight from Atomic-Resolution Electron Microscopy. *J. Am. Chem. Soc.* **2011,** *133*, 18090-18093.
(17) Lauritsen, J. V.; Besenbacher, F. Model Catalyst Surfaces Investigated by Scanning Tunneling Microscopy. *Advances in Catalysis* **2006,** *50*, 97-147.
(18) Lauritsen, J. V.; Kibsgaard, J.; Olesen, G. H.; Moses, P. G.; Hinnemann, B.; Helveg, S.; Nørskov, J. K.; Clausen, B. S.; Topsøe, H.; Lægsgaard, E., et al. Location and Coordination of Promoter Atoms in Co- and Ni-Promoted MoS_2-Based Hydrotreating Catalysts. *J. Catalysis* **2007,** *249*, 220-233.
(19) Lauritsen, J. V.; Vang, R. T.; Besenbacher, F. From Atom-Resolved Scanning Tunneling Microscopy (STM) Studies to the Design of New Catalysts. *Catal. Today* **2006,** *111*, 34-43.
(20) Cheng, W. H. Methanol and Formaldehyde Oxidation Study over Molybdenum Oxide. *J. Catal.* **1996,** *158*, 477-485.
(21) Fievez, T.; Geerlings, P.; Weckhuysen, B. M.; De Proft, F. Using DFT in Search for Support Effects During Methanol Oxidation on Supported Molybdenum Oxides. *ChemPhysChem* **2011,** *12*, 3281-3290.
(22) Kim, D. S.; Wachs, I. E.; Segawa, K. Molecular Structures and Reactivity of Supported Molybdenum Oxide Catalysts. *J. Catal.* **1994,** *149*, 268-277.
(23) Oyama, S. T.; Radhakrishnan, R.; Seman, M.; Kondo, J. N.; Domen, K.; Asakura, K. Control of Reactivity in C-H Bond Breaking Reactions on Oxide Catalysts: Methanol Oxidation on Supported Molybdenum Oxide. *J. Phys. Chem. B* **2003,** *107*, 1845-1852.
(24) Ramachandra, B.; Choi, J.; Choo, K.-Y.; Sung, J.-S.; Song, S.-D.; Kim, T.-H. Partial Oxidation of Methanol to Formaldehyde on Molybdenum Based Mixed Oxide Catalyst. *Catal. Lett.* **2005,** *105*, 23-27.
(25) Thielemann, J. P.; Hess, C. Monitoring Silica Supported Molybdenum Oxide Catalysts at Work: A Raman Spectroscopic Study. *ChemPhysChem* **2013,** *14*, 441-447.
(26) Bowker, M.; Carley, A. F.; House, M. Contrasting the Behaviour of MoO_3 and MoO_2 for the Oxidation of Methanol. *Catal. Lett.* **2008,** *120*, 34-39.
(27) Brandhorst, M.; Cristol, S.; Capron, M.; Dujardin, C.; Vezin, H.; Le bourdon, G.; Payen, E. Catalytic Oxidation of Methanol on Mo/Al_2O_3 Catalyst: An EPR and Raman/Infrared Operando Spectroscopies Study. *Catal. Today* **2006,** *113*, 34-39.
(28) Kim, H. Y.; Lee, H. M.; Pala, R. G. S.; Metiu, H. Oxidative Dehydrogenation of Methanol to Formaldehyde by Isolated Vanadium, Molybdenum, and Chromium Oxide Clusters Supported on Rutile TiO_2(110). *J. Phys. Chem. C* **2009,** *113*, 16083-16093.
(29) Routray, K.; Zhou, W.; Kiely, C. J.; Gruenert, W.; Wachs, I. E. Origin of the Synergistic Interaction between MoO_3 and Iron Molybdate for the Selective Oxidation of Methanol to Formaldehyde. *J. Catal.* **2010,** *275*, 84-98.
(30) Seman, M.; Kondo, J. N.; Domen, K.; Radhakrishnan, R.; Oyama, S. T. Reactive and Inert Surface Species Observed During Methanol Oxidation over Silica-Supported Molybdenum Oxide. *J. Phys. Chem. B* **2002,** *106*, 12965-12977.
(31) Al-Zahrani, S. M.; Jibril, B. Y.; Abasaeed, A. E. Propane Oxidative Dehydrogenation over Alumina-Supported Metal Oxides. *Ind. Eng. Chem. Res.* **2000,** *39*, 4070-4074.
(32) Bai, Z.; Li, P.; Liu, L.; Xiong, G. Oxidative Dehydrogenation of Propane over MoO_x and PO_x Supported on Carbon Nanotube Catalysts. *ChemCatChem* **2012,** *4*, 260-264.

(33) Scholz, J.; Walter, A.; Hahn, A. H. P.; Ressler, T. Molybdenum Oxide Supported on Nanostructured MgO: Influence of the Alkaline Support Properties on MoO_x Structure and Catalytic Behavior in Selective Oxidation. *Microporous Mesoporous Mater.* **2013,** *180*, 130-140.
(34) Yang, T.-J.; Lunsford, J. H. Partial Oxidation of Methanol to Formaldehyde over Molybdenum Oxide on Silica. *J. Catal.* **1987,** *103*, 55-64.
(35) Chen, K. D.; Bell, A. T.; Iglesia, E. Kinetics and Mechanism of Oxidative Dehydrogenation of Propane on Vanadium, Molybdenum, and Tungsten Oxides. *J. Phys. Chem. B* **2000,** *104*, 1292-1299.
(36) Brookes, C.; Wells, P. P.; Cibin, G.; Dimitratos, N.; Jones, W.; Morgan, D. J.; Bowker, M. Molybdenum Oxide on Fe_2O_3 Core–Shell Catalysts: Probing the Nature of the Structural Motifs Responsible for Methanol Oxidation Catalysis. *ACS Catal.* **2014,** *4*, 243-250.
(37) Koranne, M.; Goodwin, J. G.; Marcelin, G. Oxygen Involvement in the Partial Oxidation of Methane on Supported and Unsupported V_2O_5. *J. Catal.* **1994,** *148*, 378-387.
(38) Mauti, R.; Mims, C. A. Oxygen Pathways in Methane Selective Oxidation over Silica-Supported Molybdena. *Catal. Lett.* **1993,** *21*, 201-207.
(39) Tsuji, H.; Hattori, H. Oxide Surfaces That Catalyse an Acid-Base Reaction with Surface Lattice Oxygen Exchange: Evidence of Nucleophilicity of Oxide Surfaces. *ChemPhysChem* **2004,** *5*, 733-6.
(40) Mars, P.; van Krevelen, D. W. Oxidations Carried out by Means of Vanadium Oxide Catalysts. *Chem. Eng. Sci.* **1954,** *3*, 41-59.
(41) Doornkamp, C.; Ponec, V. The Universal Character of the Mars and Van Krevelen Mechanism. *J. Mol. Catal. A: Chem.* **2000,** *162*, 19-32.
(42) Vannice, M. A. An Analysis of the Mars-Van Krevelen Rate Expression. *Catal. Today* **2007,** *123*, 18-22.
(43) McFarland, E. W.; Metiu, H. Catalysis by Doped Oxides. *Chem. Rev.* **2013,** *113*, 4391-427.
(44) Paier, J.; Penschke, C.; Sauer, J. Oxygen Defects and the Surface Chemistry of Ceria: Quantum Chemical Studies Compared to Experiment. *Chem. Rev.* **2013,** *113*, 3949-3985.
(45) Carrero, C. A.; Schloegl, R.; Wachs, I. E.; Schomaecker, R. Critical Literature Review of the Kinetics for the Oxidative Dehydrogenation of Propane over Well-Defined Supported Vanadium Oxide Catalysts. *ACS Catal.* **2014,** *4*, 3357-3380.
(46) Balendhran, S.; Deng, J.; Ou, J. Z.; Walia, S.; Scott, J.; Tang, J.; Wang, K. L.; Field, M. R.; Russo, S.; Zhuiykov, S., et al. Enhanced Charge Carrier Mobility in Two-Dimensional High Dielectric Molybdenum Oxide. *Adv. Mater.* **2013,** *25*, 109-14.
(47) Lu, J.; Sun, C.; Zheng, M.; Wang, Y.; Nripan, M.; van Kan, J. A.; Mhaisalkar, S. G.; Sow, C. H. Ultrasensitive Phototransistor Based on K-Enriched MoO_3 Single Nanowires. *J. Phys. Chem. C* **2012,** *116*, 22015-22020.
(48) Mai, L. Q.; Hu, B.; Chen, W.; Qi, Y. Y.; Lao, C. S.; Yang, R. S.; Dai, Y.; Wang, Z. L. Lithiated MoO_3 Nanobelts with Greatly Improved Performance for Lithium Batteries. *Adv. Mater.* **2007,** *19*, 3712-3716.
(49) Tang, W.; Liu, L.; Zhu, Y.; Sun, H.; Wu, Y.; Zhu, K. An Aqueous Rechargeable Lithium Battery of Excellent Rate Capability Based on a Nanocomposite of MoO_3 Coated with PPy and $LiMn_2O_4$. *Energy Environ. Sci.* **2012,** *5*, 6909-6913.

(50) Wang, Z.; Madhavi, S.; Lou, X. W. D. Ultralong α-MoO_3 Nanobelts: Synthesis and Effect of Binder Choice on Their Lithium Storage Properties. *J. Phys. Chem. C* **2012,** *116*, 12508-12513.
(51) Hancox, I.; Chauhan, K. V.; Sullivan, P.; Hatton, R. A.; Moshar, A.; Mulcahy, C. P. A.; Jones, T. S. Increased Efficiency of Small Molecule Photovoltaic Cells by Insertion of a MoO_3 Hole-Extracting Layer. *Energy Environ. Sci.* **2010,** *3*, 107-110.
(52) Meyer, J.; Hamwi, S.; Kröger, M.; Kowalsky, W.; Riedl, T.; Kahn, A. Transition Metal Oxides for Organic Electronics: Energetics, Device Physics and Applications. *Adv. Mater.* **2012,** *24*, 5408-5427.
(53) Comini, E.; Yubao, L.; Brando, Y.; Sberveglieri, G. Gas Sensing Properties of MoO_3 Nanorods to CO and CO_3OH. *Chem. Phys. Lett.* **2005,** *407*, 368-371.
(54) Lupan, O.; Cretu, V.; Deng, M.; Gedamu, D.; Paulowicz, I.; Kaps, S.; Mishra, Y. K.; Polonskyi, O.; Zamponi, C.; Kienle, L., et al. Versatile Growth of Freestanding Orthorhombic α-Molybdenum Trioxide Nano- and Microstructures by Rapid Thermal Processing for Gas Nanosensors. *J. Phys. Chem. C* **2014,** *118*, 15068-15078.
(55) Sunu, S. S.; Prabhu, E.; Jayaramana, V.; Gnanasekara, K. I.; Seshagiri, T. K.; Gnanasekaran, T. Electrical Conductivity and Gas Sensing Properties of MoO_3. *Sensors and Actuators B* **2004,** *101*, 161-174.
(56) Witko, M.; Tokarz-Sobieraj, R. Surface Oxygen in Catalysts Based on Transition Metal Oxides: What Can We Learn from Cluster DFT Calculations? *Catal. Today* **2004,** *91-92*, 171-176.
(57) Coquet, R.; Willock, D. J. The (010) Surface of α-MoO_3, a DFT + U Study. *Phys. Chem. Chem. Phys.* **2005,** *7*, 3819-28.
(58) Tokarz-Sobieraj, R.; Witko, M.; Gryboś, R. Reduction and Re-Oxidation of Molybdena and Vanadia: DFT Cluster Model Studies. *Catal. Today* **2005,** *99*, 241-253.
(59) Sha, X.; Chen, L.; Cooper, A. C.; Pez, G. P.; Cheng, H. Hydrogen Absorption and Diffusion in Bulk α-MoO_3. *J. Phys. Chem. C* **2009,** *113*, 11399-11407.
(60) Lei, Y.-H.; Chen, Z.-X. DFT+U Study of Properties of MoO_3 and Hydrogen Adsorption on MoO_3(010). *J. Phys. Chem. C* **2012,** *116*, 25757-25764.
(61) Hermann, K.; Michalak, A.; Witko, M. Cluster Model Studies on Oxygen Sites at the (010) Surfaces of V_2O_5 and MoO_3. *Catal. Today* **1996,** *32*, 321-327.
(62) Michalak, A.; Hermann, K.; Witko, M. Reactive Oxygen Sites at MoO_3 Surfaces: Ab Initio Cluster Model Studies. *Surf. Sci.* **1996,** *32*, 321-327.
(63) Papakondylis, A.; Sautet, P. Ab Initio Study of the Structure of the α-MoO_3 Solid and Study of the Adsorption of H_2O and CO Molecules on Its (100) Surface. *J. Phys. Chem.* **1996,** *3654*, 10681-10688.
(64) Corà, F.; Patel, A.; Harrison, N. M.; Roetti, C.; Catlow, C. R. A. An Ab Initio Hartree–Fock Study of α-MoO_3. *J. Mater. Chem.* **1997,** *7*, 959-967.
(65) Chen, M.; Waghmare, U. V.; Friend, C. M.; Kaxiras, E. A Density Functional Study of Clean and Hydrogen-Covered α-MoO_3(010): Electronic Structure and Surface Relaxation. *J. Chem. Phys.* **1998,** *109*, 6854.
(66) Chen, M.; Friend, C. M.; Kaxiras, E. The Chemical Nature of Surface Point Defects on MoO_3(010): Adsorption of Hydrogen and Methyl. *J. Am. Chem. Soc.* **2001,** *123*, 2224-2230.

(67) Tokarz-Sobieraj, R.; Hermann, K.; Witko, M.; Blume, A.; Mestl, G.; Schlögl, R. Properties of Oxygen Sites at the MoO_3(010) Surface: Density Functional Theory Cluster Studies and Photoemission Experiments. *Surf. Sci.* **2001,** *489*, 107-125.
(68) Yin, X.; Han, H.; Miyamoto, A. Structure and Adsorption Properties of MoO_3: Insights from Periodic Density Functional Calculations. *J. Mol. Model.* **2001,** *5*, 207-215.
(69) Yan, Z.; Zuo, Z.; Lv, X.; Li, Z.; Li, Z.; Huang, W. Adsorption of NO on MoO_3 (010) Surface with Different Location of Terminal Oxygen Vacancy Defects: A Density Functional Theory Study. *Appl. Surf. Sci.* **2012,** *258*, 3163-3167.
(70) Yan, Z.; Fan, J.; Zuo, Z.; Li, Z.; Zhang, J. Nh_3 Adsorption on the Lewis and Bronsted Acid Sites of MoO_3 (010) Surface: A Cluster DFT Study. *Appl. Surf. Sci.* **2014,** *288*, 690-694.
(71) Rellán-Piñeiro, M.; López, N. The Active Molybdenum Oxide Phase in the Methanol Oxidation to Formaldehyde (Formox Process): A DFT Study. *ChemSusChem* **2015,** *8*, 2231-2239.
(72) Tahini, H. A.; Tan, X.; Lou, S. N.; Scott, J.; Amal, R.; Ng, Y. H.; Smith, S. C. Mobile Polaronic States in α-MoO_3 : An Ab Initio Investigation of the Role of Oxygen Vacancies and Alkali Ions. *ACS Appl. Mater. Interfaces* **2016,** *8*, 10911-10917.
(73) Agarwal, V.; Metiu, H. Energy of Oxygen-Vacancy Formation on Oxide Surfaces: Role of the Spatial Distribution. *J. Phys. Chem. C* **2016,** *120*, 2320-2323.
(74) Andersson, G.; Magneli, A. On the Crystal Structure of Molybdenum Trioxide. *Acta Chem. Scand.* **1950,** *4*, 793-797.
(75) Kihlborg, L. Least Squares Refinement of the Crystal Structure of Molybdenum Trioxide. *Arkiv för Kemi* **1963,** *21*, 357-364.
(76) Brandt, B.; Skapski, A. A Refinement of the Crystal Structure of Molybdenum Dioxide. *Acta Chem. Scand.* **1967,** *21*, 661-672.
(77) Magnéli, A.; Andersson, G. On the MoO_2 Structure Type. *Acta Chem. Scand.* **1955,** *9*, 1378-1381.
(78) Goodenough, J. Metallic Oxides. *Prog. Solid State Chem.* **1971,** *5*, 145-399.
(79) Kresse, G.; Hafner, J. Ab Initio Molecular Dynamics for Liquid Metals. *Phys. Rev. B* **1993,** *47*, 558-561.
(80) Kresse, G.; Hafner, J. Ab Initio Molecular-Dynamics Simulation of the Liquid-Metal–Amorphous-Semiconductor Transition in Germanium. *Phys. Rev. B* **1994,** *49*, 14251-14269.
(81) Kresse, G.; Furthmüller, J. Efficiency of Ab-Initio Total Energy Calculations for Metals and Semiconductors Using a Plane-Wave Basis Set. *Comput. Mater. Sci.* **1996,** *6*, 15-50.
(82) Kresse, G.; Furthmuller, J. Efficient Iterative Schemes for Ab Initio Total-Energy Calculations Using a Plane-Wave Basis Set. *Phys. Rev. B* **1996,** *54*, 11169-11186.
(83) Perdew, J. P.; Burke, K.; Ernzerhof, M. Generalized Gradient Approximation Made Simple. *Phys. Rev. Lett.* **1996,** *77*, 3865-3868.
(84) Blöchl, P. E. Projector Augmented-Wave Method. *Phys. Rev. B* **1994,** *50*, 17953-17979.
(85) Frenkel, D.; Smit, B. *Understanding Molecular Simulation: From Algorithms to Applications*; Academic Press Inc.: San Diego CA, 2002.
(86) Grimme, S. Semiempirical GGA-Type Density Functional Constructed with a Long-Range Dispersion Correction. *J. Comput. Chem.* **2006,** *27*, 1787-99.
(87) Dudarev, S.; Botton, G.; Savrasov, S. Electron-Energy-Loss Spectra and the Structural Stability of Nickel Oxide: An LSDA+ U Study. *Phys. Rev. B* **1998,** *57*, 1505-1509.

(88) Heyd, J.; Scuseria, G. E.; Ernzerhof, M. Hybrid Functionals Based on a Screened Coulomb Potential. *J. Chem. Phys.* **2003,** *118*, 8207.
(89) Paier, J.; Marsman, M.; Hummer, K.; Kresse, G.; Gerber, I. C.; Angyán, J. G. Screened Hybrid Density Functionals Applied to Solids. *J. Chem. Phys.* **2006,** *124*, 154709.
(90) Paier, J.; Marsman, M.; Hummer, K.; Kresse, G.; Gerber, I. C.; Ángyán, J. G. Erratum: "Screened Hybrid Density Functionals Applied to Solids" [J. Chem. Phys. 124, 154709 (2006)]. *J. Chem. Phys.* **2006,** *125*, 249901.
(91) Henkelman, G.; Arnaldsson, A.; Jónsson, H. A Fast and Robust Algorithm for Bader Decomposition of Charge Density. *Comput. Mater. Sci.* **2006,** *36*, 354-360.
(92) Baldoni, M.; Craco, L.; Seifert, G.; Leoni, S. A Two-Electron Mechanism of Lithium Insertion into Layered α-MoO_3: A DFT and DFT+U Study. *J. Mater. Chem. A* **2013,** *1*, 1778.
(93) Getsoian, A. B. B.; Bell, A. T. The Influence of Functionals on Density Functional Theory Calculations of the Properties of Reducible Transition Metal Oxide Catalysts. *J. Phys. Chem. C* **2013,** *117*, 25562-25578.
(94) Hautier, G.; Ong, S. P.; Jain, A.; Moore, C. J.; Ceder, G. Accuracy of Density Functional Theory in Predicting Formation Energies of Ternary Oxides from Binary Oxides and Its Implication on Phase Stability. *Phys. Rev. B* **2012,** *85*, 155208.
(95) Lutfalla, S.; Shapovalov, V.; Bell, A. T. Calibration of the DFT/GGA+U Method for Determination of Reduction Energies for Transition and Rare Earth Metal Oxides of Ti, V, Mo, and Ce. *J. Chem. Theory Comput.* **2011,** *7*, 2218-2223.
(96) Wang, F.; Pang, Z.; Lin, L.; Fang, S.; Dai, Y.; Han, S. Origin of Magnetism in Undoped MoO_2 Studied by First-Principles Calculations. *Phys. Rev. B* **2010,** *81*, 134407.
(97) Gruber, H.; Haselmair, H.; Fritzer, H. P. On Magnetic Properties of Some Molybdenum Oxides. *J. Solid State Chem.* **1983,** *47*, 84-91.
(98) Khilla, M.; Mikhail, H. Magnetic Susceptibility of Molybdenum Trioxide, Dioxide and Some Suboxides. *Czech. J. Phys.* **1980,** *30*, 1039-1045.
(99) Røst, E. A Magnetic Investigation on Supported Molybdenum Dioxide. *J. Am. Chem. Soc.* **1959,** *81*, 3843-3845.
(100) Coey, J. M. D.; Roux-Buisson, H.; Brusetti, R. The Electronic Phase Transitions in FeS and NiS. *J. Phys. Colloques* **1976,** *37*, C4-1-C4-10.
(101) Smith, M. R.; Ozkan, U. S. The Partial Oxidation of Methane to Formaldehyde: Role of Different Crystal Planes of MoO_3. *J. Catal.* **1993,** *141*, 124-139.
(102) Floquet, N.; Bertrand, O.; Heizmann, J. Structural and Morphological Studies of the Growth of MoO_3 Scales During High-Temperature Oxidation of Molybdenum. *Oxid. Met.* **1992,** *37*, 253-280.
(103) Deskins, N. A.; Rousseau, R.; Dupuis, M. Defining the Role of Excess Electrons in the Surface Chemistry of TiO_2. *J. Phys. Chem. C* **2010,** *114*, 5891-5897.
(104) Chrétien, S.; Metiu, H. Electronic Structure of Partially Reduced Rutile TiO_2 (110) Surface: Where Are the Unpaired Electrons Located? *J. Phys. Chem. C* **2011,** *2*, 4696-4705.
(105) Ganduglia-Pirovano, M. V.; Da Silva, J. L. F.; Sauer, J. Density-Functional Calculations of the Structure of near-Surface Oxygen Vacancies and Electron Localization on CeO_2(111). *Phys. Rev. Lett.* **2009,** *102*, 1-4.

(106) Li, H. Y.; Wang, H. F.; Gong, X. Q.; Guo, Y. L.; Guo, Y.; Lu, G.; Hu, P. Multiple Configurations of the Two Excess 4f Electrons on Defective CeO_2 (111): Origin and Implications. *Phys. Rev. B* **2009,** *79*, 2-5.
(107) Choi, J.-G.; Thompson, L. T. XPS Study of As-Prepared and Reduced Molybdenum Oxides. *Appl. Surf. Sci.* **1996,** *93*, 143-149.
(108) Haber, J.; Lalik, E. Catalytic Properties of MoO_3 Revisited. *Catal. Today* **1997,** *33*, 119-137.
(109) Mendelovici, L.; Lunsford, J. Partial Oxidation of Ethane to Ethylene and Acetaldehyde over a Supported Molybdenum Catalyst. *J. Catal.* **1985,** *50*, 37-50.
(110) Spevack, P. A.; McIntyre, N. S. Thermal Reduction of MoO_3. *J. Phys. Chem.* **1992,** *96*, 9029-9035.
(111) Dyrek, K.; Łabanowska, M. Electron Paramagnetic Resonance Investigation of the Paramagnetic Centres in Polycrystalline MoO_3. *J. Chem. Soc., Faraday Trans.* **1991,** *87*, 1003-1009.
(112) Mei, D.; Karim, A. M.; Wang, Y. Density Functional Theory Study of Acetaldehyde Hydrodeoxygenation on MoO_3. *J. Phys. Chem. C* **2011,** *115*, 8155-8164.
(113) Smith, M. R.; Ozkan, U. S. Transient Isotopic Labeling Studies under Steady-State Conditions in Partial Oxidation of Methane to Formaldehyde over MoO_3 Catalysts. *J. Catal.* **1993,** *142*, 226-236.
(114) Andersson, A.; Hansen, S. Catalytic Anisotropy of MoO_3 in the Oxidative Ammonolysis of Toluene. *J. Catal.* **1988,** *346*, 332-346.
(115) Hernandez, R. A.; Ozkan, U. S. Structural Specificity of Molybdenum Trioxide in C4 Hydrocarbon Oxidation. *Industrial & Engineering Chemistry Research* **1990,** *29*, 1454-1459.
(116) Queeney, K.; Friend, C. Site-Selective Surface Reactions: Hydrocarbon Oxidation Processes on Oxidized Mo (110). *J. Phys. Chem. B* **2000,** *104*, 0-6.
(117) Tatibouet, J.; Germain, J. A Structure-Sensitive Oxidation Reaction: Methanol on Molybdenum Trioxide Catalysts. *J. Catal.* **1981,** *378*, 375-378.
(118) Tatibouet, J.; Phichitkul, C.; Germain, J. Structure-Sensitive Catalytic Oxidation of Butenes on Molybdenum Trioxide Crystallites. *J. Catal.* **1986,** *234*, 231-234.
(119) Chase, M. W.; Davies, C. A.; Downey, J. R.; Frurip, D. J.; McDonald, R. A.; Syverud, A. N. NIST JANAF Thermochemical Tables 1985 Version 1.0. *National Institute of Standards and Technology Gaithersburg, MD 20899* **1985**.

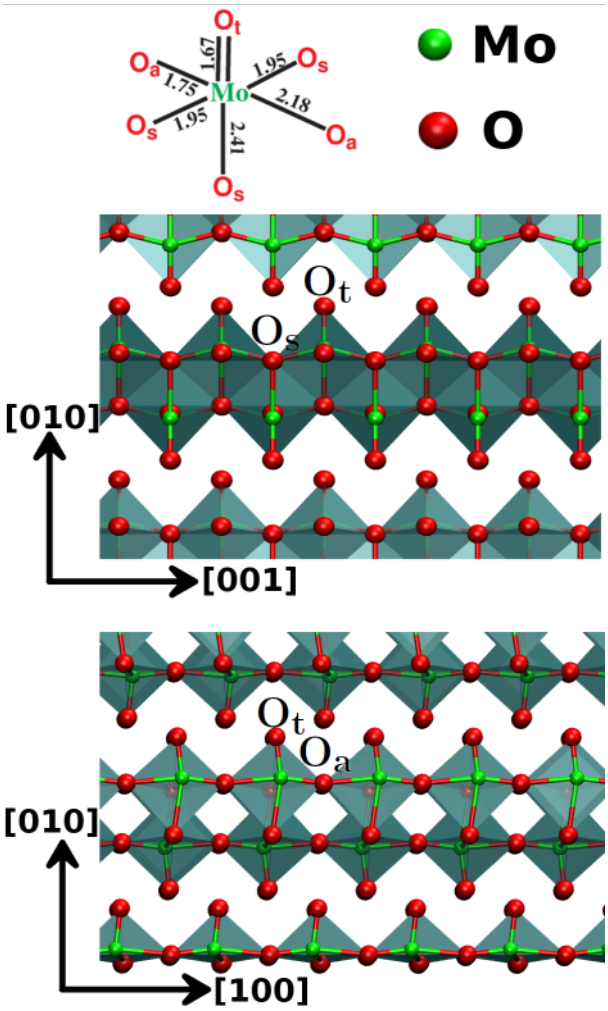

Figure 1: Two views of crystal structure of bulk α-MoO_3. [MoO_6] octahedra are shown in green. The bond lengths in one [MoO_6] octahedron are given at the top. The bilayers are clearly visible in the structure. For an interactive 3D model of MoO_3 see Figure S11 in the Supporting Information.

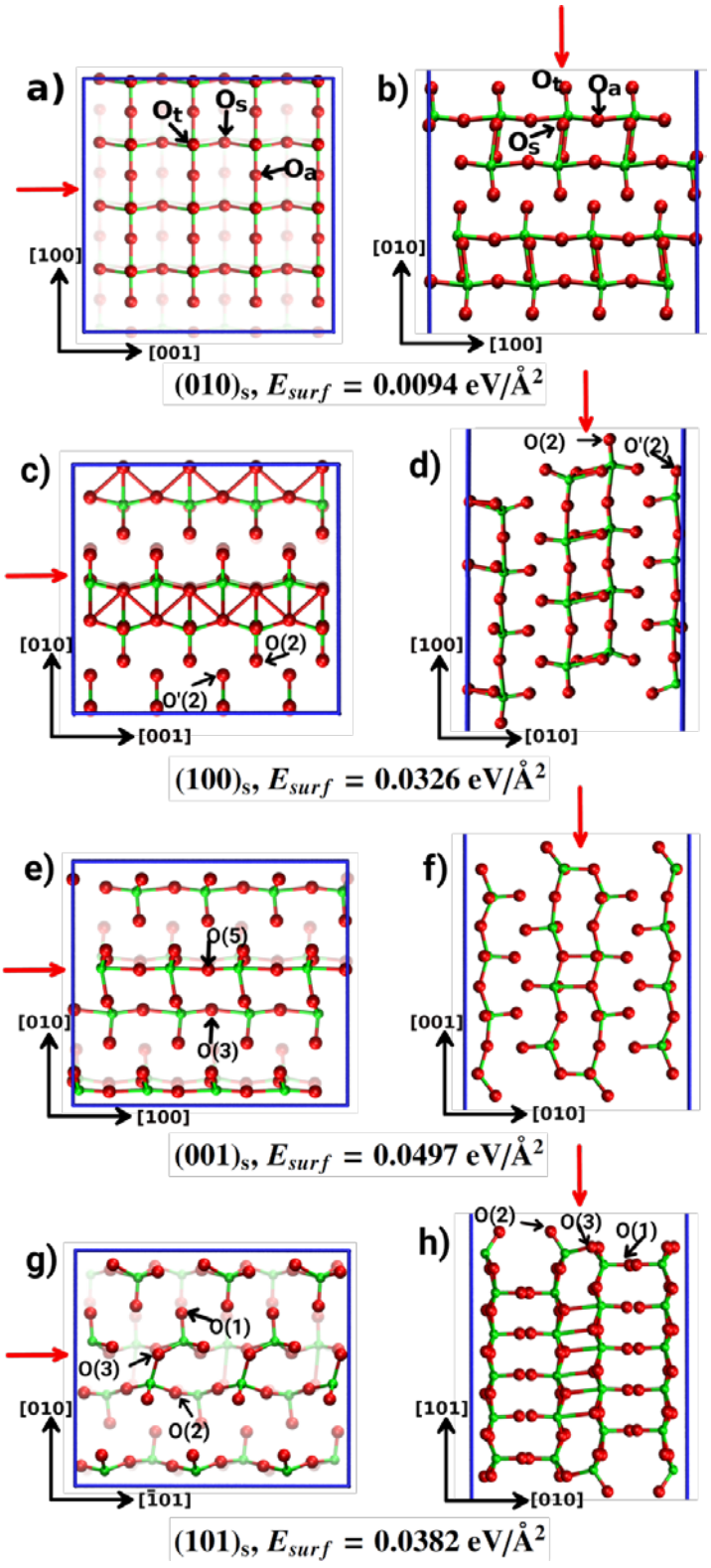

Figure 2: The structures of the slabs studied here. The four drawings in the left column show the slab surfaces viewed when looking down towards the surface (top view). The right column shows a side-view of the slabs. The red arrow indicates the direction of view in the adjacent

image. The blue line indicates the direction in which the structure is periodically repeated. A missing blue border indicates where the slab borders the vacuum. Mo atoms are green and oxygen is red. We use the intensity of the color to give depth perception: the atoms that are farther from the reader have lower color saturation. The faces are **(a,b)** $(010)_s$, **(c,d)** $(100)_s$, **(e,f)** $(001)_s$, and **(g,h)** $(101)_s$. For each face we give the surface energy E_{surf}. The energy of oxygen-vacancy formation was calculated only for the vacancies formed by removing the oxygen atoms labeled in the figures. For example, oxygen vacancy was studied for O(3) and O(5) on slab $(001)_s$. These oxygen atoms are easiest to remove for the corresponding ribbon. For each slab, we provide interactive 3D model in the Supporting Information, Figure S12.

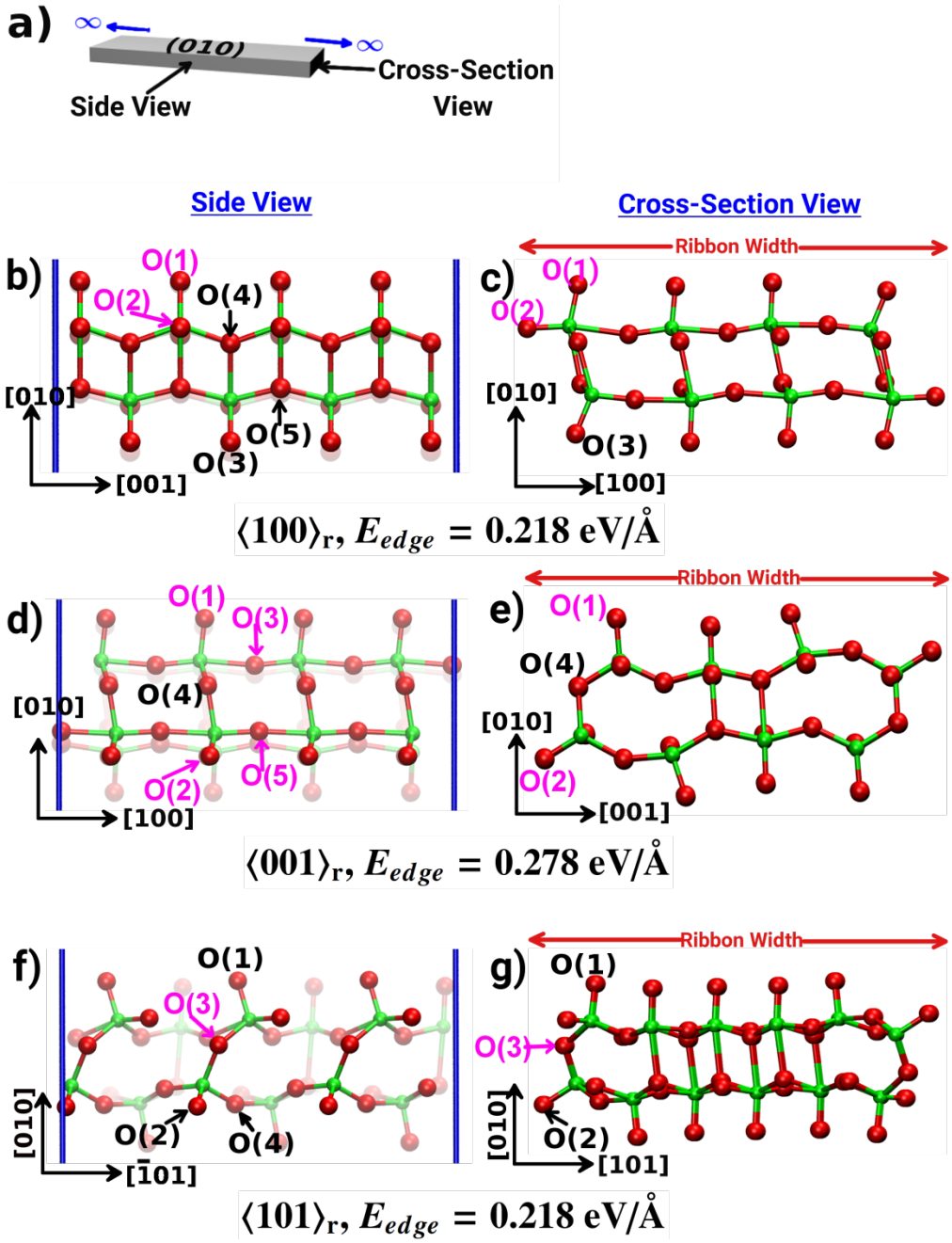

Figure 3: a) Schematic figure of an infinite 2-dimensional ribbon. The structure is periodically repeated in the direction marked cross-section view and it is finite in the direction marked side view. The structures in the left panel show side views of different ribbons. The blue lines show the directions in which a structure is periodically repeated. If no blue line is present the structure borders to vacuum. For example, in the Figure (b) the system is infinite in the [001] direction and finite in the [010] and [100] directions. The figure in (c) is infinite in the direction facing the viewer and finite in the other two directions. We have only studied the oxygen-vacancies formed by removing the oxygen atoms that are labelled in the figure by the symbols O(n), n = 1, . . , 5. The label of the oxygen atoms that are easier to remove are in magenta and the labels on the ones

that are hard to remove are in black. The Mo atoms are green and the oxygen atoms are red. Layers farther from the viewer are fainter. For each ribbon, we provide an interactive 3D model in the Supporting Information, Figure S13.

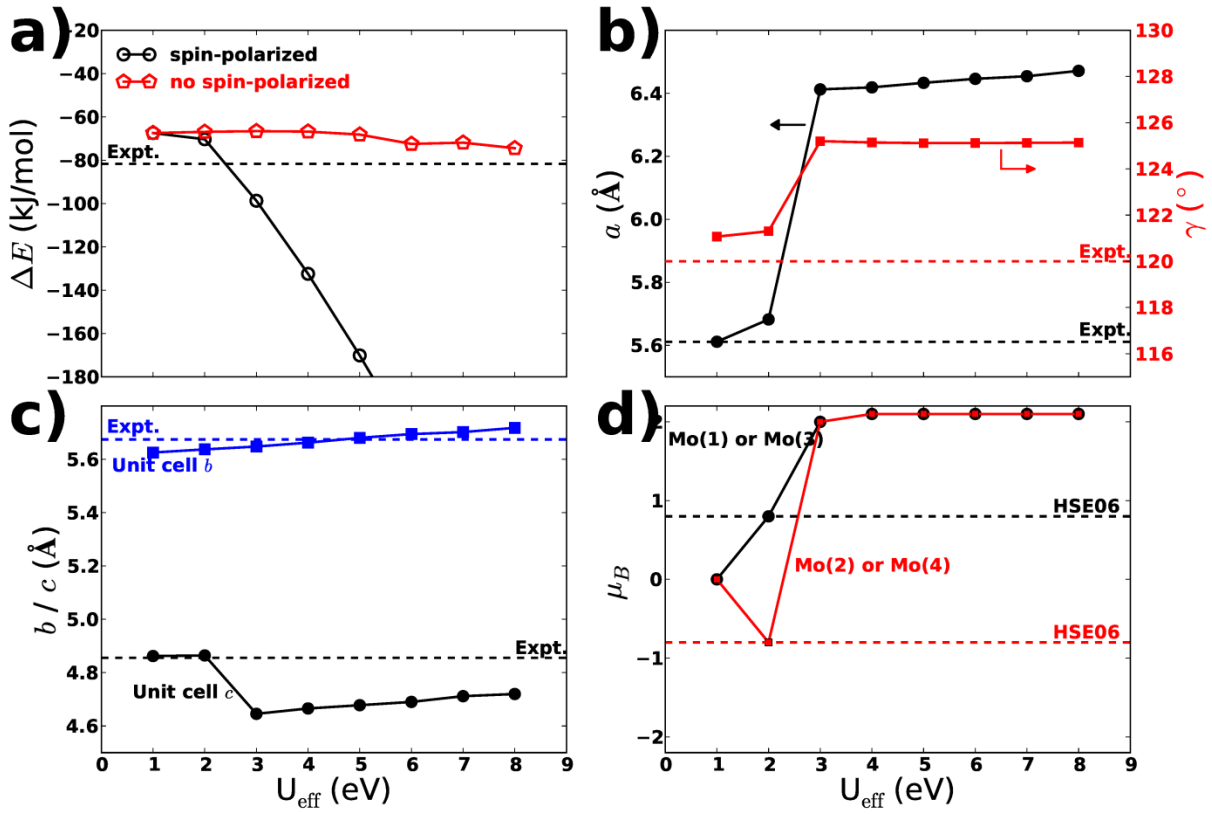

Figure 4: (**a)** Effect of U_{eff} on ΔE of the reaction $MoO_3 + H_2 \rightarrow MoO_2 + H_2O$. Experimental value for this reaction (at 0 K) was obtained from the NIST JANAF tables.[119] Effect of U_{eff} on: **(b)** lattice parameters a and γ of MoO_2,(**c)** lattice parameters b and c of MoO_2, and (**d)** magnetic moments of four Mo atoms in the unit cell of MoO_2. [Mo(1), Mo(2)] and [Mo(3), Mo(4)] are the pairs of atoms involved in shorter metal-metal bond.

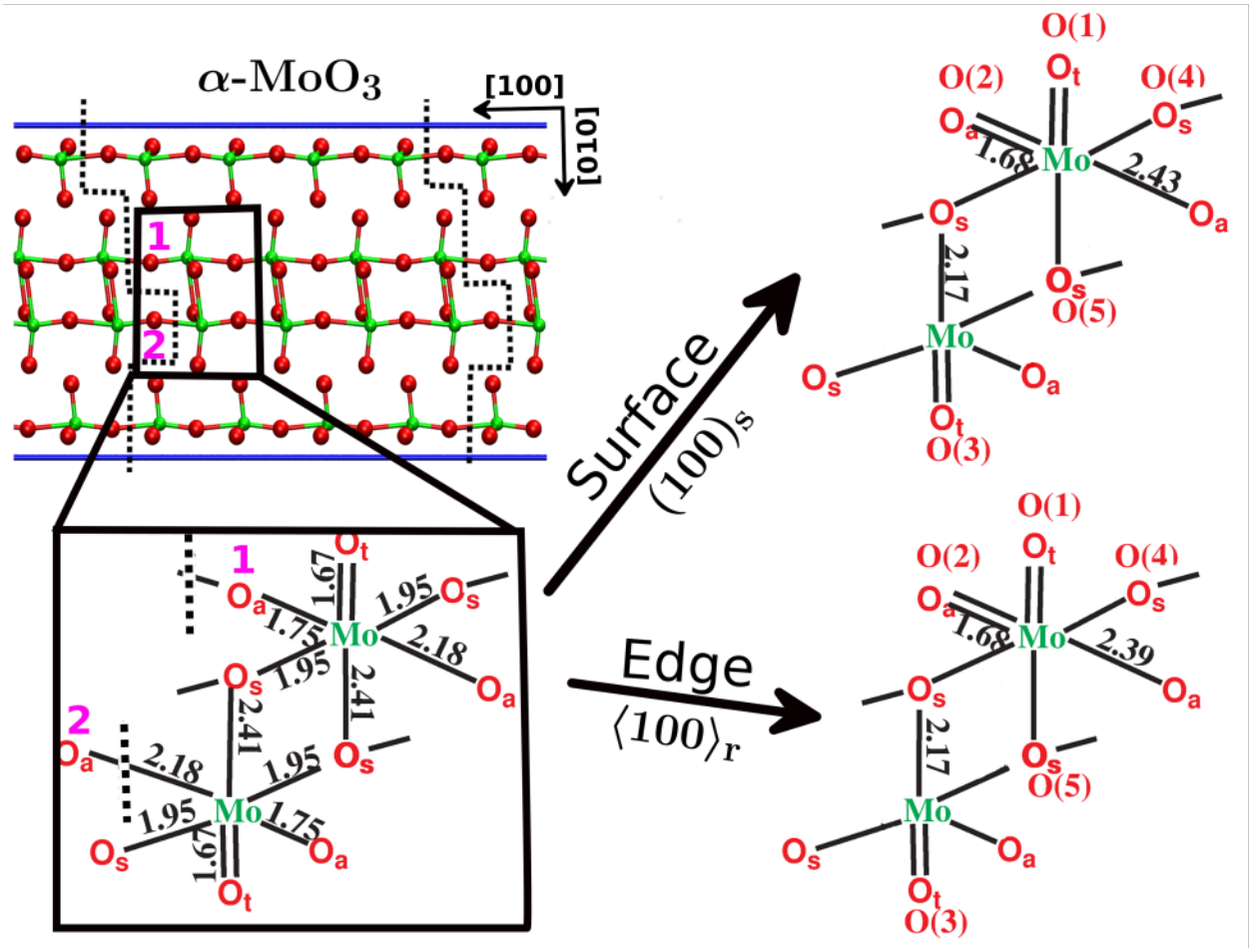

Figure 5: Schematic figure of bond lengths in bulk α-MoO_3 (left), relaxed <100>$_r$ edge (right bottom), and relaxed $(100)_s$ surface (right top). For clarity only two [MoO_6] octahedra in different (010) sub-layers are shown. We represent cuts with dotted lines. Mo are shown in green and oxygen in red. The oxygens numbered with parentheses (on surface and edge) correspond those labelled in Figure 2c and Figure 3b.

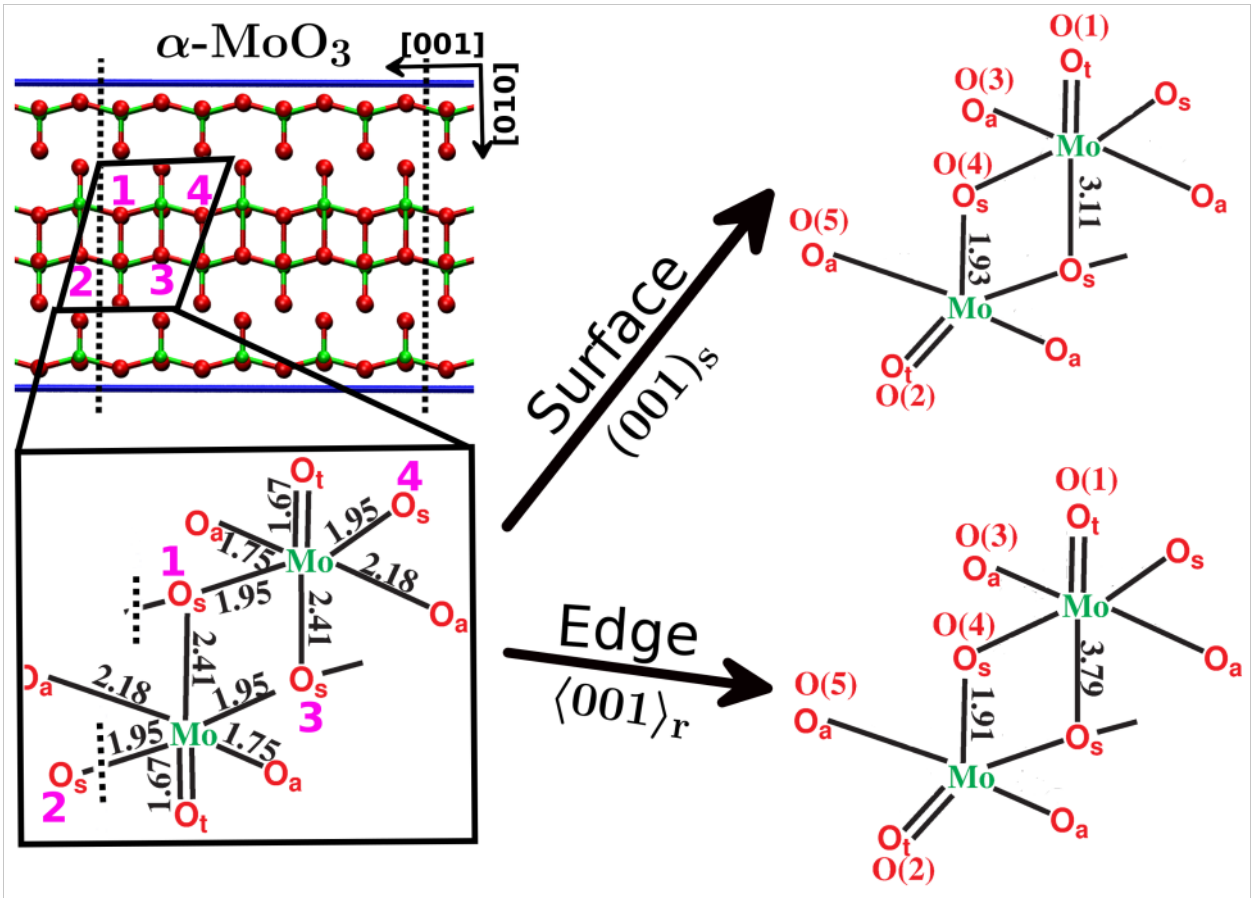

Figure 6: Schematic figure of bond lengths in bulk α-MoO_3 (left), relaxed <001>$_r$ edge (right bottom), and relaxed $(001)_s$ surface (right top). For clarity only two [MoO_6] octahedra in different (010) sub-layers are shown. The cuts are shown with dotted lines. Mo are shown in green and oxygen in red. The oxygens numbered with parentheses (on surface and edge) correspond to those labelled in Figure 2e and Figure 3d.

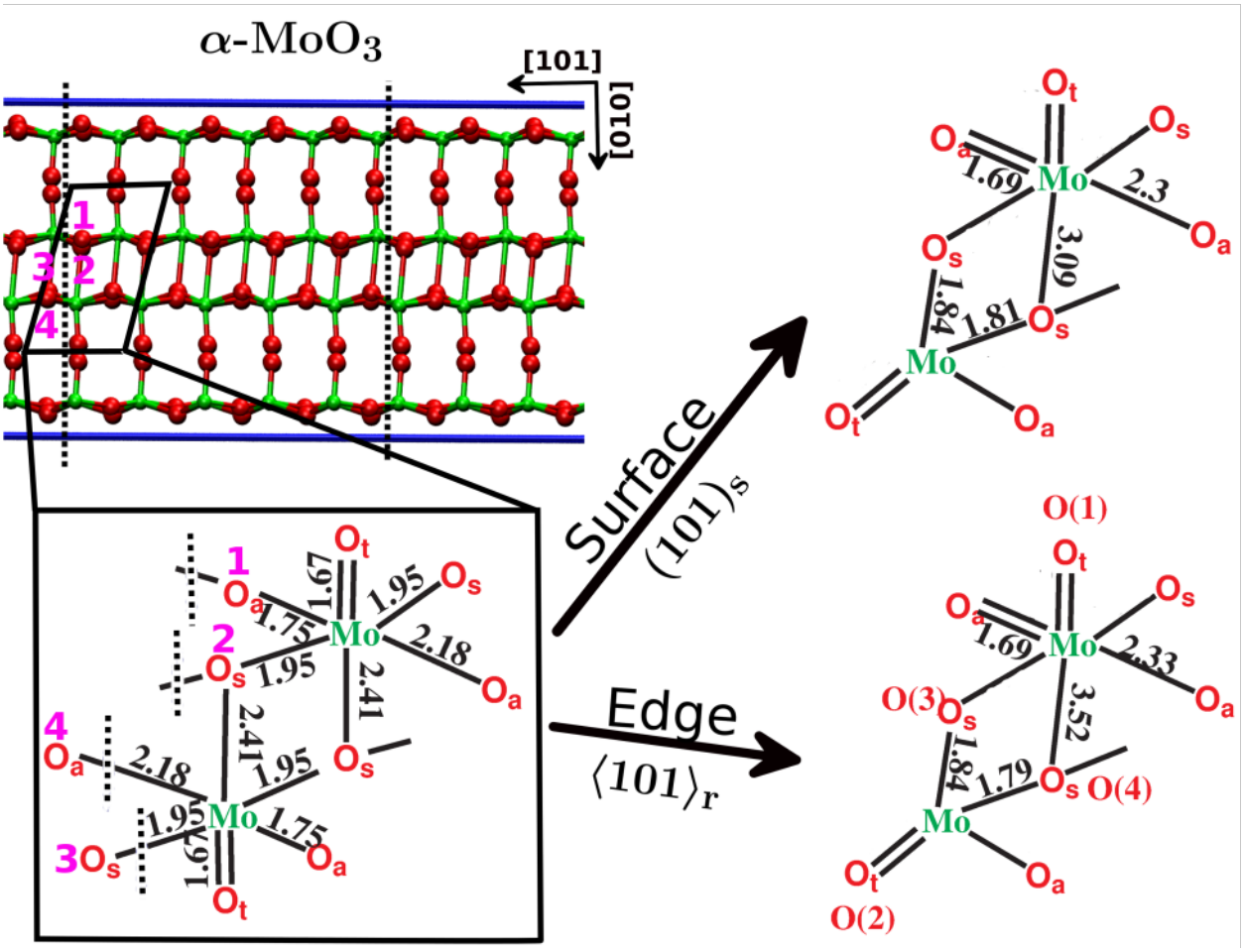

Figure 7: Schematic figure of bond lengths in bulk α-MoO_3 (left), relaxed <101>$_r$ edge (right bottom), and relaxed $(101)_s$ surface (right top). For clarity only two [MoO_6] octahedra in different (010) sub-layers are shown. The cuts are shown with dotted lines. Mo are shown in green and oxygen in red. The oxygens numbered with parentheses (on surface and edge) correspond to those labelled in Figure 2g and Figure 3f.

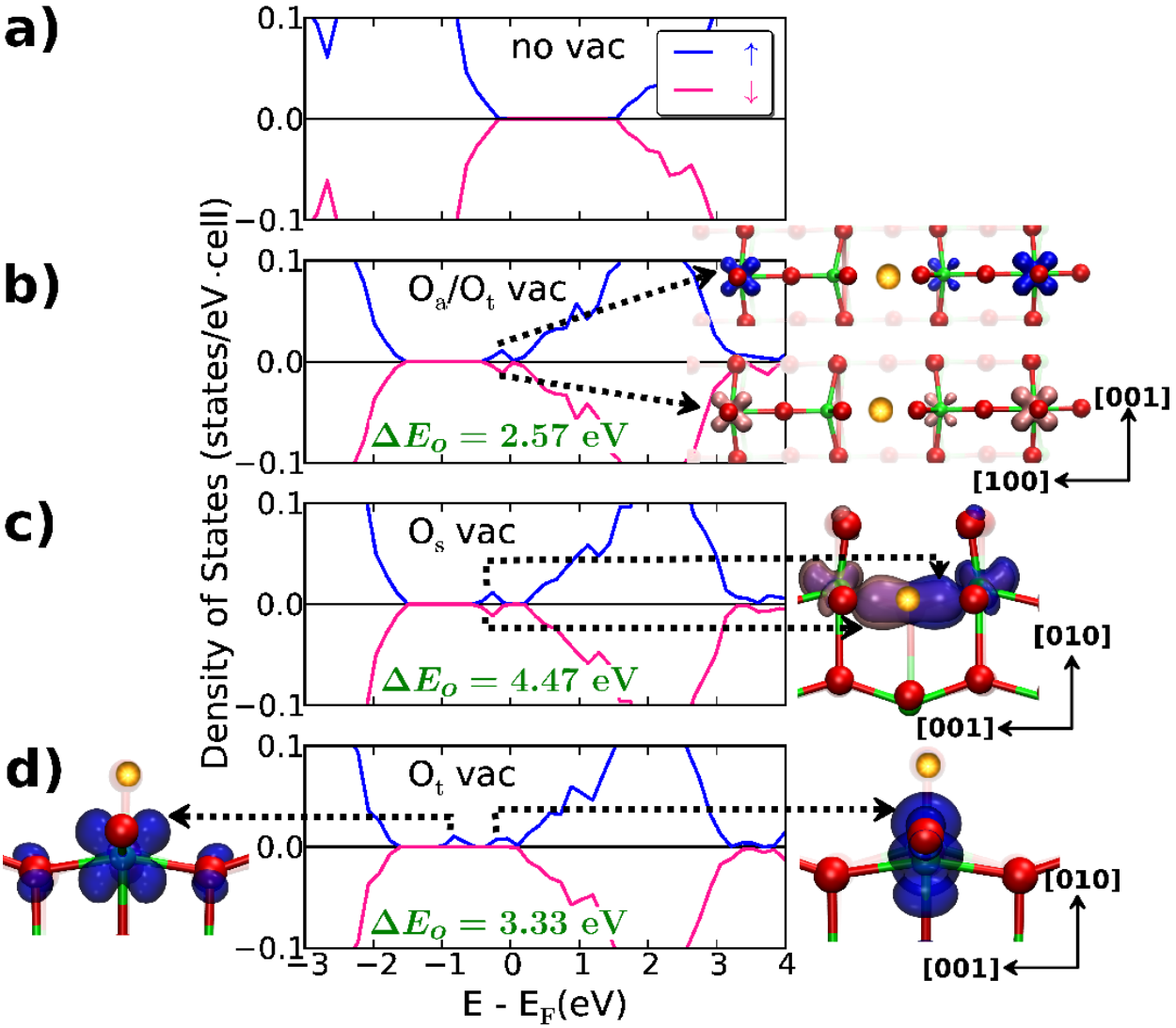

Figure 8: Density of states (DOS) for a stoichiometric $(010)_s$ bilayer and for the same bilayer with oxygen vacancies at various sites. (**a)** DOS of a stoichiometric, single bilayer $(010)_s$ sheet. (**b)** DOS for the same bilayer with an oxygen vacancy formed by removing O_a or O_t. (**c)** DOS when vacancy is formed by removing O_s. (**d)** DOS for alternative, higher energy structure, in which the oxygen vacancy was formed by removing O_t. For each vacancy, partial charge densities of HOMOs are also shown, for an isovalue of 0.05 e/Å^3. The yellow sphere represents the position of the oxygen removed. We also show oxygen-vacancy formation energies for generating a ½O_2.

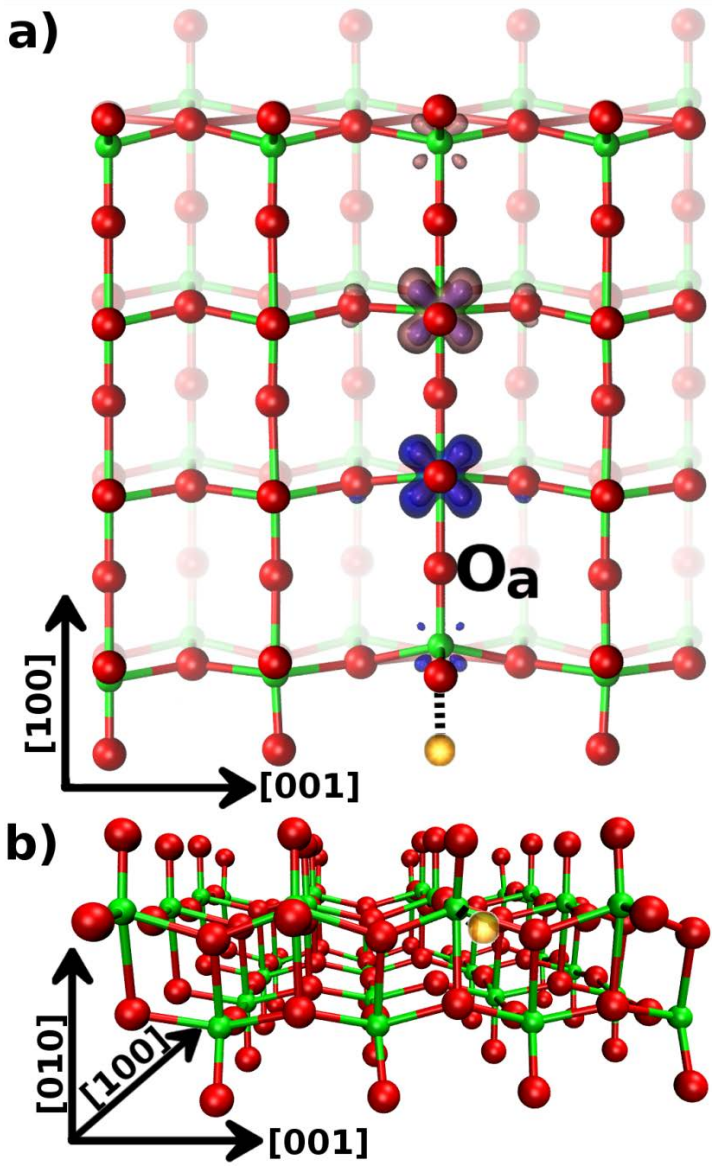

Figure 9: (**a)** Top view along (010) direction (the exfoliating direction) of $<100>_r$ with O(2) vacancy. Layers farther from the viewer are fainter. Also shown are the partial charge densities of states in the energy gap for an isovalue of 0.05 e/Å^3. The yellow sphere represents the position of the oxygen removed. (**b)** Side view of $<100>_r$ with O(2) vacancy. Mo are shown in green and oxygen in red.

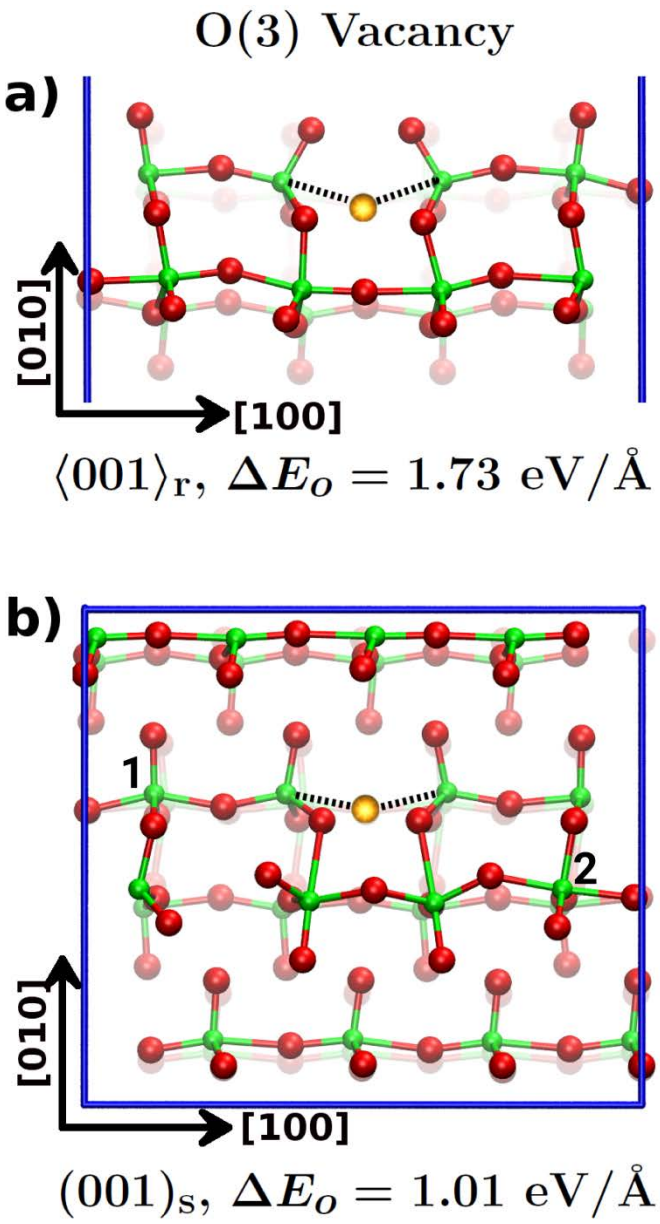

Figure 10: (**a)** Side view of <001>$_r$ with O(3) vacancy. For definition of side view of <001>$_r$ see Figure 3a. (**b)** Top view of $(001)_s$ with O(3) vacancy. Note that side view of <001>$_r$ ribbon corresponds to completely exfoliated top view of $(001)_s$ slab along [010] direction. We also report O(3) vacancy formation energies required to generate a ½O_2 molecule. Layers farther from the viewer are fainter. Mo are shown in green and oxygen in red. The oxygen removed is shown by yellow sphere. The bonds broken are shown with dotted lines. The Mo atoms numbered '1' and '2' in Figure (b) are the atoms where the two electrons localizes after O(3) removal for $(001)_s$. For clarity, we have not shown the partial density of states.

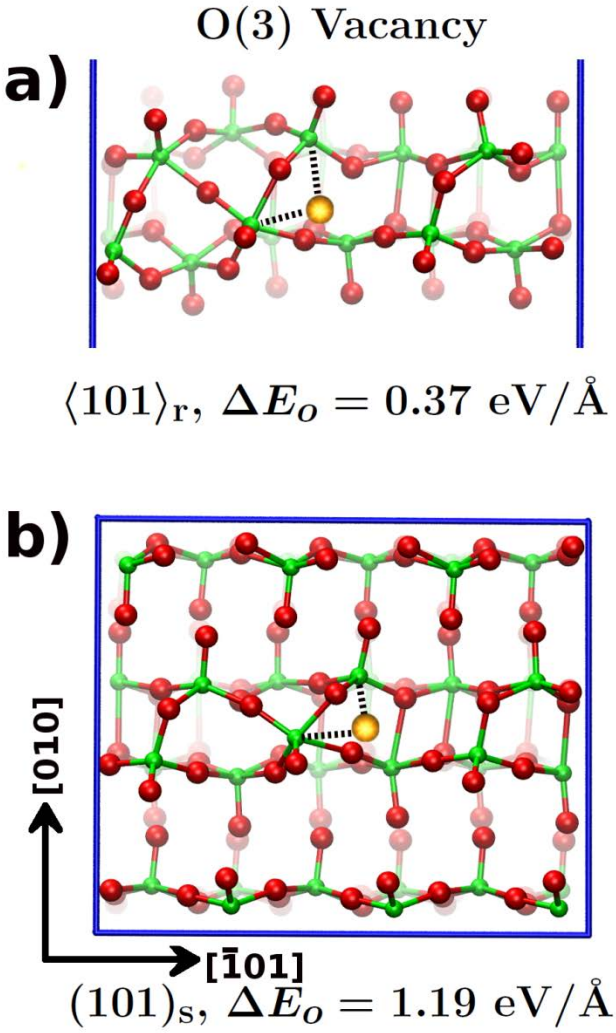

Figure 11: (a) Side view of <101>$_r$ with O(3) vacancy and **(b)** top view of $(101)_s$ O(3) vacancy. Note that side view of <101>$_r$ ribbons corresponds to completely exfoliated top view of $(001)_s$ slabs along [010] direction. Layers farther from the viewer are fainter. We also report O(3) vacancy formation energies required to generate a ½O_2 molecule. Mo are shown in green and oxygen in red. The oxygen removed is shown by yellow sphere and the bonds broken are shown with dotted lines. In Supporting Information (Figure S7), we also provide final optimized structures of O(1) and O(2) vacant surfaces and edges.

Table 1: Cell parameters of α-MoO_3 crystal evaluated at U_{eff} =2 eV.

Lattice Parameter	Expt.[75]	PBE+U	% Error
a (Å)	3.96	3.90	1.5
b (Å)	13.86	13.91	0.4
c (Å)	3.69	3.70	0.3

Table 2: Bond lengths and Bader charges of bulk and exfoliated bilayers of α-MoO_3.

	Expt.	Bulk	1-bilayer	2-bilayer
Bond Lengths (Å)				
Mo-O_t	1.67	1.67	1.67	1.67
Mo-O_s	1.95	1.93	1.95	1.95
Mo-O_t	1.74, 2.25	1.79, 2.18	1.76, 2.18	1.75, 2.18
Bader Charges				
Mo		2.67	2.68	2.65
O_t		-0.69	-0.68	-0.68
O_s		-1.07	-1.07	-1.06
O_a		-0.91	-0.93	-0.92

Table 3: Oxygen vacancy formation energies required to form a ½O_2 molecule by removal of oxygen from surfaces and edges. For oxygen numbering refer to **Figure 2** and **Figure 3**. Here we only provide lowest vacancy formation energies. For a complete list see Supporting Information Table S1. We use subscript 'r' to denote ribbons and 's' to denote slabs. We use the word sheet to denote a single bilayer of MoO_3 which extends to infinity in two directions. We also give state of *two* electrons left after oxygen removal.

Oxygens Removed		***ΔEo* (eV)**		**Electron Localization**	
(010) Faces					
	Model	**2D-Sheet**	**Slab**	**2D-Sheet**	**Slab**
O_a or O_t	$(010)_s$	2.57	2.57	Delocalized	Delocalized
(100) Face and Edge					
		$<100>_r$	**$(100)_s$**	**$<100>_r$**	**$(100)_s$**
O(1)		2.08[a]	-	2 Mo^{5+}	-
O(2)		2.08[a]	2.06 (2.13)[b]	2 Mo^{5+}	2 Mo^{5+}
(001) Face and Edge					
		$<001>_r$	**$(001)_s$**	**$<001>_r$**	**$(001)_s$**
O(1)		1.73[c]	-	Delocalized	-
O(2)		1.50[d]	-	Delocalized	-
O(3)		1.73[c]	1.01	Delocalized	2 Mo^{5+}
O(5)		1.50[d]	1.29	Delocalized	2 Mo^{5+}
(101) Face and Edge					
		$<101>_r$	**$(101)_s$**	**$<101>_r$**	**$(101)_s$**
O(3)		0.37	1.19	Delocalized	Delocalized

[a] On optimization O(1) and O(2) vacancy yields the same final state.

[b] The value in parentheses is for removing O'(2).

[c] On optimization O(1) and O(3) vacancy yields the same final state.

[d] On optimization O(2) and O(5) vacancy yields the same final state.